Multiscale approach to geo-composite cellular structures subjected to rock impacts

François Nicot, Philippe Gotteland, David Bertrand, Stéphane Lambert

Multiscale approach to geo-composite cellular structures subjected to rock impacts

François Nicot[1, 4, *, †], Philippe Gotteland[2, 4], David Bertrand[1, 2, 3, 4] and Stéphane Lambert[1, 2, 4]

[1]Cemagref, Unité de Recherche Erosion Torrentielle Neige et Avalanches, Grenoble, France
[2]LIRIGM, UJF, Grenoble, France
[3]France-Macaferri, Valence, France
[4]RNVO Group: Research Network on Natural Hazards and Vulnerability of Structures, France

Geo-composite cellular structures are an efficient technological solution for various applications in civil engineering. This type of structure is particularly well adapted to resisting rockfalls and can act as a defensive structure. However, the design of such structures is for the most part empirically based; this lack of research-based design stagnates optimization and advanced development. In this paper, the mechanical behaviour of a geo-composite cellular structure is investigated using a multi-scale approach, from the individual cell made up of an assembly of rocky particles contained in a wire netting cage to the entire structure composed of a regular array of cells. Based on discrete modelling of both the cell and structure scales, a computational tool has been developed for design purposes.

Keywords: discrete element method; elasto-plastic behaviour; granular materials; mechanical interaction; wire structure; protective-reinforced structure; multi-scale approach

1. INTRODUCTION

1.1. General scope

In most mountainous areas, rockfalls are by far the most recurrent and prejudicial phenomena that interact with the human environment: damage to roads, civil engineering constructions including

*Correspondence to: François Nicot, Cemagref, Unité de Recherche Erosion Torrentielle Neige et Avalanches, Grenoble, France.
†E-mail: francois.nicot@grenoble.cemagref.fr

Contract/grant sponsor: France-Macaferri
Contract/grant sponsor: RNVO
Contract/grant sponsor: PGRN

Figure 1. Examples of damage to civil infrastructures.

buildings and infrastructures, sometimes loss of human life (Figure 1). Because of the complexity of mountain sides, made up of a succession of talus slopes and rocky cliffs, it is often not possible to prevent the phenomenon from occurring. Thus, protecting people and infrastructures requires designing and installing adequate defensive structures. Such structures must be able to resist rockfall impacts, whose incident kinetic energy may vary within a large range, from less than 1 kJ up to 50 000 kJ and beyond [1]. In this context, it seems relevant to propose deformable structures that are able to dissipate a large part of the impacting boulder's incident energy from the specific behaviour of the constitutive materials. This goal can be achieved by considering geo-composite cellular structures, which can be regarded as a reinforced dam whose front part is made up of an assembly of metallic cages, hereafter referred to as gabion cells, filled with materials such as gravel, stones, or sand placed in an appropriately designed geosynthetic bag, or adapted material such as a composite material. The remainder of the structure is usually designed as a standard embankment by including reinforcement elements that ensure that the back face is sufficiently steep. Throughout this paper, the front face of the structure denotes the side oriented towards the upstream slope, whereas the opposite back part faces downstream (Figure 2).

During impacts, large deformation within cells, which can be regarded as a mesoscopic homogeneous elementary unit, is likely to occur together with relative displacements between adjoining cells, thereby increasing energy dissipation. In the present study, cells are filled with calibrated (limestone) rocky particles. Of course, other constitutive materials can also be considered, and important research is now in progress to extend the proposed approach to other types of filling geomaterials including specific man-made materials such as tyre pieces [2].

There is a pressing need today to improve the understanding of the mechanical behaviour of such protective structures during an impact [3–6]. This is a necessary stage in designing these structures properly, analysing the influence of a particular innovative concept from both technological and mechanical points of view, which finally contributes to the development of more highly optimized structures. The overall mechanical response of a geo-composite cellular structure is highly dependent on the behaviour of each constituent on smaller scales, such as the gabion cells. Hence, the model presented in this paper is based on a multiscale approach that makes it possible to investigate the response of a structure on a macroscopic scale by accounting for the determinant properties of constitutive materials on both microscopic and mesoscopic scales. Herein,

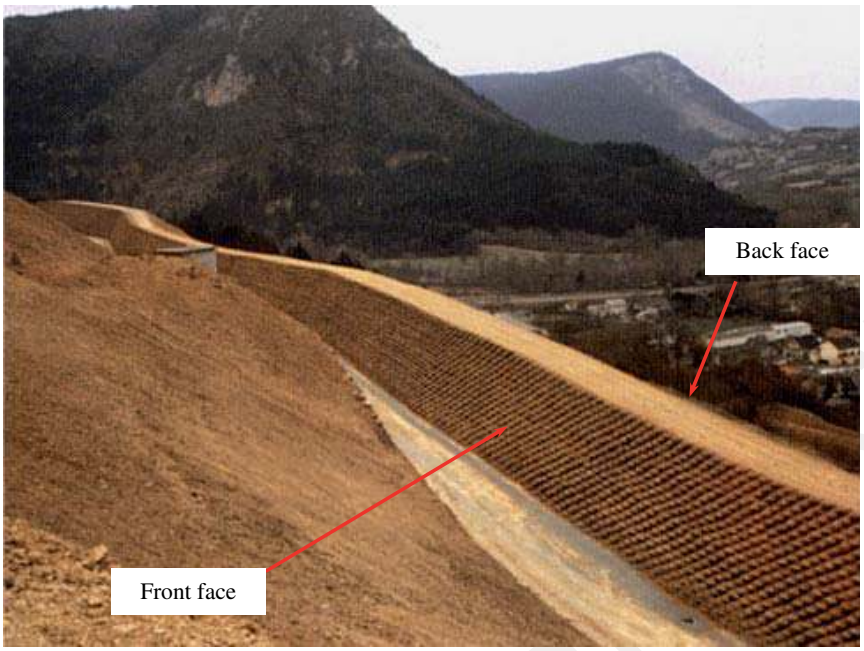

Figure 2. Example of a geo-composite embankment.

the mesoscopic scale corresponds to the gabion cell scale. The rocky particles, the basic element of the gabion cell, can be regarded as the microscopic scale of the problem at hand (Figure 3). Such approaches are now known to be powerful in dealing with structures that exhibit a discrete nature on different successive scales (see for instance, [7–9]). This type of approach has also given rise to a promising alternative method to those based on phenomenological approaches to describing the behaviour of granular assemblies. Emerging in the 1970s [10–17], micro-mechanical approaches have been highly successful for roughly 10 years. High-performance computer-assisted methods make it possible to implement adequate statistical tools that are well adapted to granular media (see for instance, [18–24]).

The discrete nature of the structure, on the different scales relevant to the problem treated herein, warrants a discrete element method be used. The discrete element method generally applies to a collection of bodies that interact with each other in contact interactions. Each body is described as a rigid element subjected to body forces and contact forces occurring when this element comes into contact with a neighbouring element. The motion of each element is determined by solving the balance equations, which yields the location of the elements by time integration. Contact forces are computed from a specific description of the contact (for an overview, see [25]). The procedure adopted by PFC^{3D} software [26] relates the incremental normal and tangential interaction forces between two elements that are not necessarily in contact (remote interaction) with the incremental normal and tangential relative displacements of the interacting elements through specific constitutive relations. These relations account for the behavioural specificities of the material. In the approach presented in this paper, the computational software PFC^{3D} was employed to describe the constitutive behaviour of gabion cells, including both the wire netting box and the filling material. Then this computational tool was used again to simulate the response of the entire structure. Developing an operational tool for engineering purposes within the same

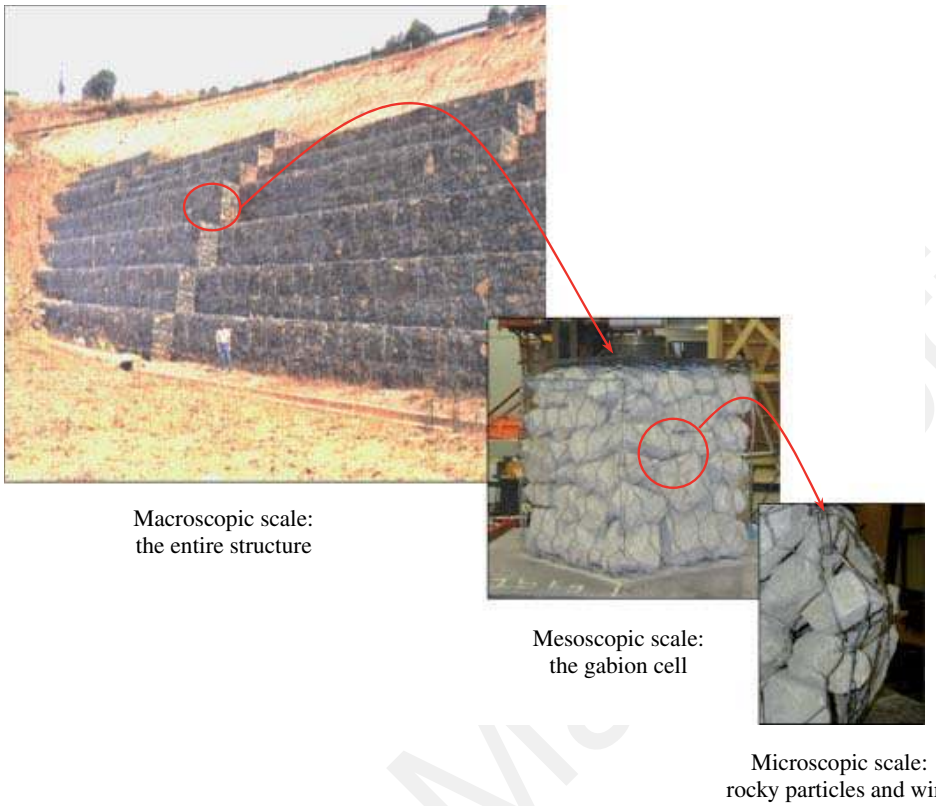

Figure 3. Multiscale approach: from rocky particles to the entire structure.

computational environment on all the relevant scales of the problem is a striking feature of this approach.

This paper first investigates the mechanical behaviour of the gabion cell by considering the filling material and the wire netting cage, both in interaction. Then the complete structure made up of several contiguous cells is considered. Parametric analyses are presented to investigate the influence of the initial kinetic energy of the boulder, and preliminary conclusions are drawn on the residual capacity of a geo-composite cellular structure after successive impacts.

2. MECHANICAL MODELLING OF A SINGLE CELL

Gabion cells are made up of a wire netting box wrapping the filling material composed of an assembly of rocky particles. The wire netting box is required to maintain the filling material inside the cell. As illustrated in Figure 4, the wire netting is composed of a regular mesh of both intersected single and double twisted elementary metallic wires. During the deformation of the cell, rocky particles move and interact with the wire netting box, which is thus strained. As a consequence, the mechanical response of a single cell over a loading programme results from the response of the wire netting box and the filling material, both in close interaction. Hence, it is necessary to describe the two materials in combination. In this section, the case of the wire netting box is considered first.

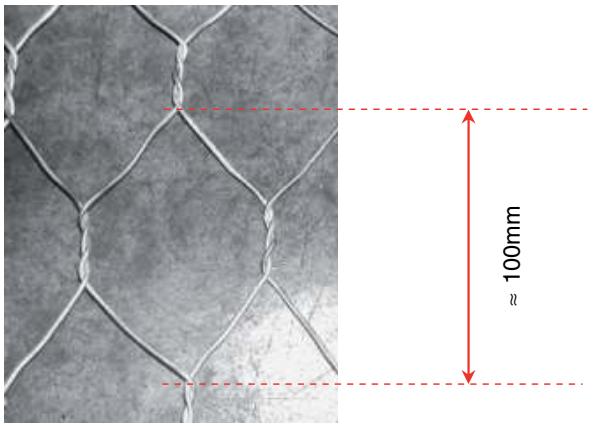

Figure 4. The wire mesh of the box. Single and double twisted wires.

2.1. *The wire netting box*

2.1.1. Spatial description. As wires that constitute the box are short with respect to the characteristic size of the box (i.e. less than 10%), it can be assumed that each elementary wire retains a straight line between two intersection points when the box is strained. Thus, bending effects are not present (the case of a wire net sheet subjected to an in-plane compressive loading is ignored). Moreover, as usually assumed for off-plane loaded wire nets, shear and torsion mechanisms are considered as second-order mechanisms. Even though the discrete element method [27] was initially dedicated to describing granular assemblies with multiple interactions, it also extends to other types of material that can be represented by a set of individual nodes. This approach is particularly convenient to manage the occurrence of large strains. Following an approach previously adopted to model wire structures [3, 7, 8, 28, 29], the wire netting box can be described by a set of nodes located at the intersection points between the wires (Figure 5). The dotted lines between the nodes are fictitious. In this approach, the wire net is replaced with a mesh of nodes (or elements). The behaviour of the constitutive metal is taken into account by introducing adequate interacting laws between adjoining nodes.

2.1.2. Constitutive model in finite strains. Each pair of adjoining nodes, at the extremities of a dotted line (Figure 5(b)), is subjected to an internal force. This force models the mechanical strength of the wire that exists between the two connection extremities described by two nodes. The constitutive model must give the changes in the forces along the different fictitious dotted lines of the mesh as a function of their lengthening in the tensile regime. In the compressive regime, the force will be set to zero.

2.1.2.1. Case of a single wire. The constitutive model of a single wire in the tensile regime is developed in the usual framework of elasto-plasticity [30]. This model expresses the changes in the incremental tensile force $\mathrm{d}F$ that exist in a wire of initial length l^s as a function of its incremental lengthening $\mathrm{d}x$. For an incremental lengthening $\mathrm{d}x$, $\mathrm{d}x_\mathrm{e}$ is the incremental elastic lengthening and $\mathrm{d}x_\mathrm{p}$ is the incremental plastic lengthening: $\mathrm{d}x = \mathrm{d}x_\mathrm{e} + \mathrm{d}x_\mathrm{p}$. Furthermore, x_p is chosen as the hardening parameter, and $\hat{R}^s(x_\mathrm{p})$ is the plastic yield. The yielding function f_t^s is defined by the yielding criterion $f_\mathrm{t}^s(F, \hat{R}^s) = F - \hat{R}^s(x_\mathrm{p}) = 0$. For a given state after a given loading, characterized

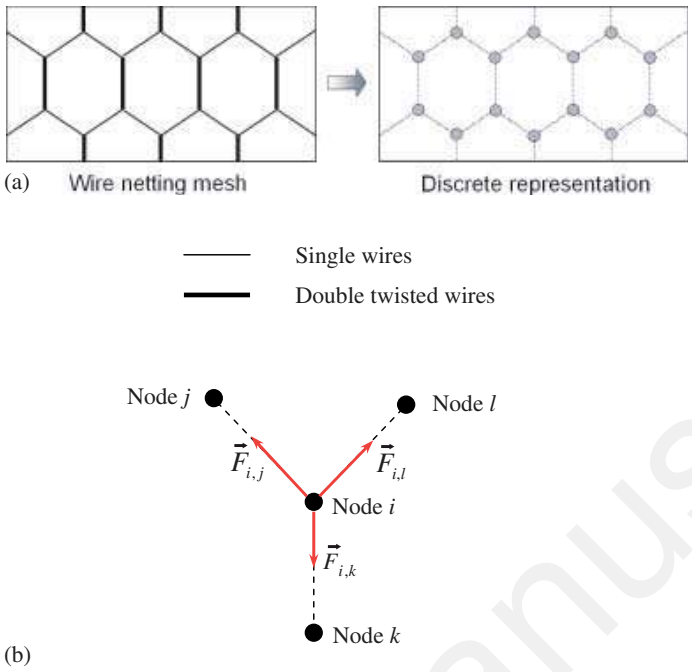

Figure 5. Spatial description of the wire netting by using a discrete element method (a) and interaction of a wire netting node with the adjoining nodes (b).

by (x_p, F), two cases can be distinguished. The behaviour is reputed elastic if either the condition $f_t^s(F, \hat{R}^s) < 0$ or the condition $f_t^s(F, \hat{R}^s) = 0$ with $dx < 0$ fulfilled. In that case:

$$dF = k_e^{s,t}\, dx_e \tag{1}$$

$$dx_e = \frac{1}{k_e^{s,t}}\, dF \tag{2}$$

$$dx_p = 0 \tag{3}$$

where $k_e^{s,t}$ denotes the tensile elastic stiffness for a single wire. On the contrary, if the condition $f_t^s(F, \hat{R}^s) = 0$ with $dx > 0$ is fulfilled, then the behaviour is elasto-plastic and both elastic and plastic strains occur:

$$dx_e = \frac{1}{k_e^{s,t}}\, dF \tag{4}$$

and

$$dx_p = \frac{1}{(d\hat{R}^s/dx_p)}\, dF \tag{5}$$

with

$$dF = \frac{k_e^{s,t}(d\hat{R}^s/dx_p)}{k_e^{s,t} + d\hat{R}^s/dx_p} dx \tag{6}$$

In addition, failure occurs if the total tensile strain ε^s within the wire, defined by the relation $x = l^s \varepsilon^s$, exceeds a limit value $\varepsilon^s_{\text{lim}}$. The proposed constitutive model requires the identification of both functions $\hat{R}^s(x_\text{p})$ and $\mathrm{d}\hat{R}^s/\mathrm{d}x_\text{p}$, as well as the calibration of parameters $k_\text{e}^{s,\text{t}}$ and $\varepsilon^s_{\text{lim}}$. This can be achieved by considering the tensile curve $\sigma^s(\varepsilon)$ relating both axial strain ε and axial stress σ^s obtained from an experimental tensile test carried out on a single wire (for a detailed presentation, see Bertrand *et al*. [31]).

It must be emphasized that Equations (1)–(6) are general in the sense that any loading path (including loading, unloading, reloading) can be treated.

2.1.2.2. Constitutive relations for a double twisted wire. The particular structure of the double twisted wire, which can be regarded as two enlaced helical wires, makes tensile tests very difficult. In particular, it is very difficult to experimentally reproduce how a double twisted wire is loaded within a wire netting. Given the lack of experimental investigations on double twisted wires, further assumptions are required, so it will be assumed herein that the model developed for a single wire can be formally extended to the case of a double twisted wire by introducing adequate quantities $\hat{R}^d(x_\text{p})$, $\mathrm{d}\hat{R}^d/\mathrm{d}x_\text{p}$, $k_\text{e}^{d,\text{t}}$ and $\varepsilon^d_{\text{lim}}$. Functions $\hat{R}^d(x_\text{p})$ and $\mathrm{d}\hat{R}^d/\mathrm{d}x_\text{p}$ can be calibrated from the tensile curve $\sigma^d(\varepsilon)$ relating the axial stress σ^d to the axial strain ε. By denoting $\hat{\varepsilon}_\text{e}$ the common initial elastic limit for both the single wire and the double twisted wire, the original stress–strain tensile curves $\sigma^s(\varepsilon)$ and $\sigma^d(\varepsilon)$ associated with these materials are assumed to be homothetic to one another with respect to the stress within the range $[0; \hat{\varepsilon}_\text{e}]$, and with respect to both strain and stress beyond $\hat{\varepsilon}_\text{e}$. Thus:

If $\varepsilon \in [0; \hat{\varepsilon}_\text{e}]$:

$$\sigma^d(\varepsilon) = \frac{k_\text{e}^{d,\text{t}}}{k_\text{e}^{s,\text{t}}} \sigma^s(\varepsilon) \tag{7}$$

If $\varepsilon > \hat{\varepsilon}_\text{e}$:

$$\sigma^d(\varepsilon) = \frac{k_\text{e}^{d,\text{t}}}{k_\text{e}^{s,\text{t}}} \sigma^s(\varepsilon') \tag{8}$$

with

$$\varepsilon' = \hat{\varepsilon}_\text{e} + \frac{\varepsilon^s_{\text{lim}} - \hat{\varepsilon}_\text{e}}{\varepsilon^d_{\text{lim}} - \hat{\varepsilon}_\text{e}} (\varepsilon - \hat{\varepsilon}_\text{e}) \tag{9}$$

where the failure strain $\varepsilon^d_{\text{lim}}$ is equal to the failure strain $\varepsilon^s_{\text{lim}}$ reduced by a coefficient $\lambda_\varepsilon < 1$: $\varepsilon^d_{\text{lim}} = \lambda_\varepsilon \varepsilon^s_{\text{lim}}$. This is justified by the fact that constructing a double twisted wire from two single wires induces local strains that can be responsible for strain hardening. Thus, each wire constituting the double twisted wire has certainly undergone plastic strains, so that the amplitude of the strain range before failure is more restricted.

Since the double twisted wire, of length l^d, can be regarded as an assembly of two overlapping helical wires, the elastic stiffness $k_\text{e}^{d,\text{t}}$ of the double twisted wire is assumed to range between two values: a lower value corresponding to the stiffness of an element composed of two independent helical wires, regarded as two independent, parallel springs, and an upper value corresponding to the stiffness of two parallel single wires of length l^d. As a consequence, if we denote k_h the elastic

stiffness of a single helical wire, the initial elastic stiffness $k_e^{d,t}$ of the double twisted wire can be computed as follows:

$$k_e^{d,t} = 2(\lambda_k k_h + (1 - \lambda_k) k_e^{s,t}) \tag{10}$$

where λ_k is a weight parameter. The calculation of the stiffness of a helical wire is now the subject of analysis. Let us consider a helical wire, and let us denote l its height, R the radius of the spiral, N_t the number of turns, d the diameter of the wire, E the Young modulus and v Poisson's ratio of the constitutive material. It is well known in cable mechanics that the elastic stiffness k_h of the helical wire can be given by [32]:

$$\frac{1}{k_h} = \frac{128N(1+v)R^3\cos\alpha}{Ed^4}\left(1 + \frac{5}{36}\left(\frac{d}{R}\right)^2 + \frac{\tan^2\alpha}{1+v} + \frac{\tan^2\alpha}{16(1+v)}\left(\frac{d}{R}\right)^2\right) \tag{11}$$

with $\tan\alpha = l/2\pi NR$.

It must be emphasized that Equation (11) takes into account tensile, bending, shear, and torsion mechanisms that occur together during the traction of a helical wire.

In the particular case of the double twisted wire considered herein, we have $R = d$, as well as $N = 1.5$. By denoting l^d the length of the double twisted wire, it follows that:

$$k_h = \frac{Ed}{48\cos\alpha(\frac{41}{9}(1+v) + \frac{17}{4}\tan^2\alpha)} \tag{12}$$

with $\tan\alpha = l^d/3\pi d$.

As for single wires, it is assumed that in the compressive regime $k_e^{d,c} = 0$.

2.1.3. Using the PFC^{3D} *environment.* As described in Sections 2.1.1 and 2.1.2, modelling the wire netting can be integrated within the PFC^{3D} environment. For this purpose, the nodes that describe the wire netting are placed in their initial configuration, which depend on the initial shape and geometry of the box. A spherical discrete element is affected to each node. Then a contact map is created, associating with each node (or element) a given set of adjoining nodes (or elements). Finally, under any prescribed external loading, the PFC^{3D} solving process computes all the internal forces between each pair of adjoining elements at each time step. These forces are accounted for when the second Newton law is applied to each wire netting element. The displacement of each element can be computed by solving balance equations, yielding the current strained configuration of the wire net at each stage of the loading. For this purpose, specific algorithms have been developed in the programming language FISH [26]. The FISH command SET FISHCALL was used to calculate the internal forces at each time step.

2.1.4. Calibration of the constitutive models for the wire netting box. The constitutive model developed for both single and double twisted wires introduces two parameters: λ_ε and λ_k. These parameters can be calibrated from the comparison between the experimental and numerical responses of a plane net sheet subjected to a given loading programme. A series of two-dimensional experimental tensile tests was therefore carried out on a plane wire net sheet. During the tests, the two lateral sides were free to move, whereas the bottom side was maintained blocked and the upper side was subjected to a controlled axial displacement x_a (Figure 7). The net sheet was 500 mm in height and 1000 mm in width. The mesh size was 8–10 mm, as defined in Figure 6,

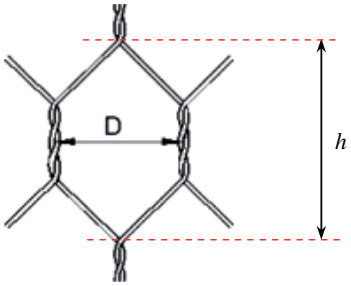

Figure 6. Definition of mesh sizes. An 8- to 10-mm mesh size means that $D = 8$ mm and $h = 10$ mm.

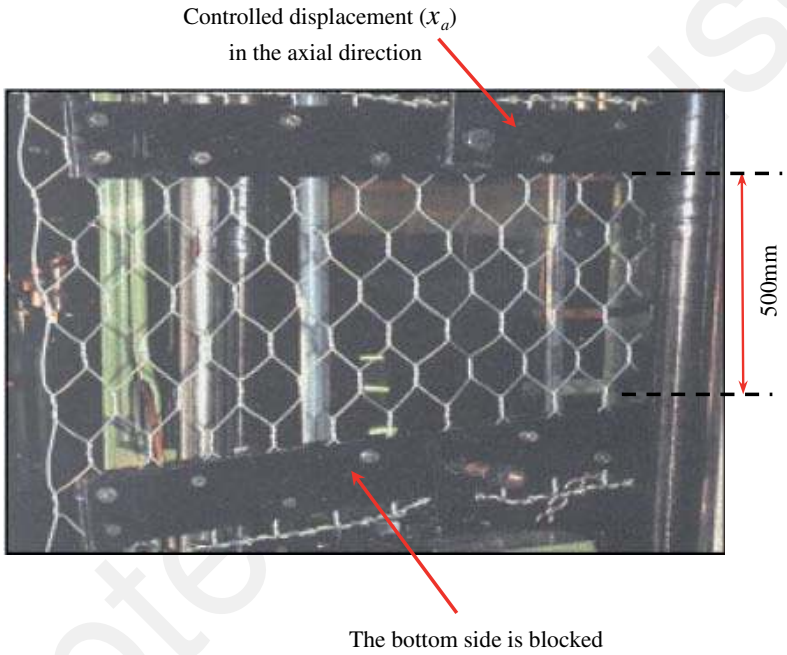

Figure 7. Tensile test: initial shape of the wire net sheet.

with a wire 2.7 mm in diameter. For a given axial displacement x_a of the upper side, the resulting axial force F_a applied to the upper side was recorded.

This experimental test was simulated respecting the loading procedure. The horizontal bottom elements were fixed, whereas the upper elements were subjected to a constant velocity displacement in the axial direction. Lateral particles were free to move. The simulation was pursued until a complete failure of the net sheet took place (Figure 8). The resulting axial tensile force F_a was computed by adding the resulting axial forces acting on each horizontal bottom element, and the controlled axial displacement x_a of the frame was recorded. The curve giving the changes in F_a *versus* x_a is depicted in Figure 9, showing that satisfactory agreement between both experimental and numerical results was obtained for the values $\lambda_\varepsilon = 0.4$ and $\lambda_k = 0.66$. Henceforth, these values will be adopted for the simulations presented throughout this paper.

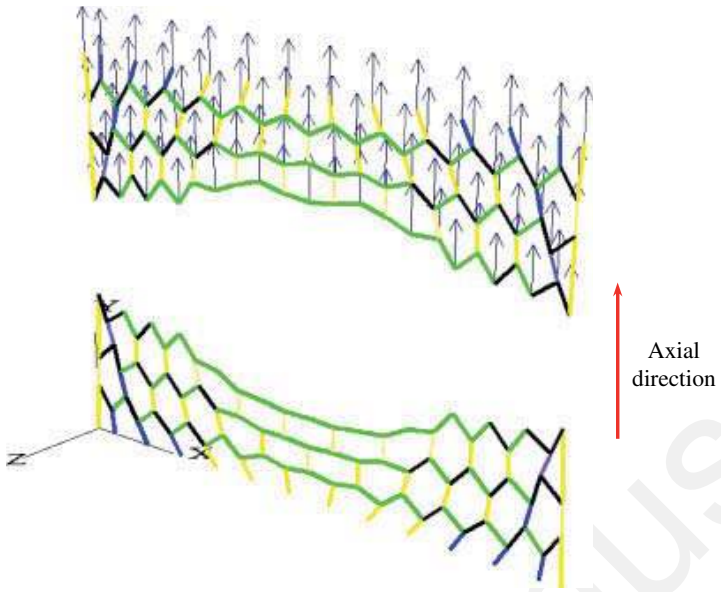

Figure 8. Strain pattern within the wire net sheet when complete failure is reached.

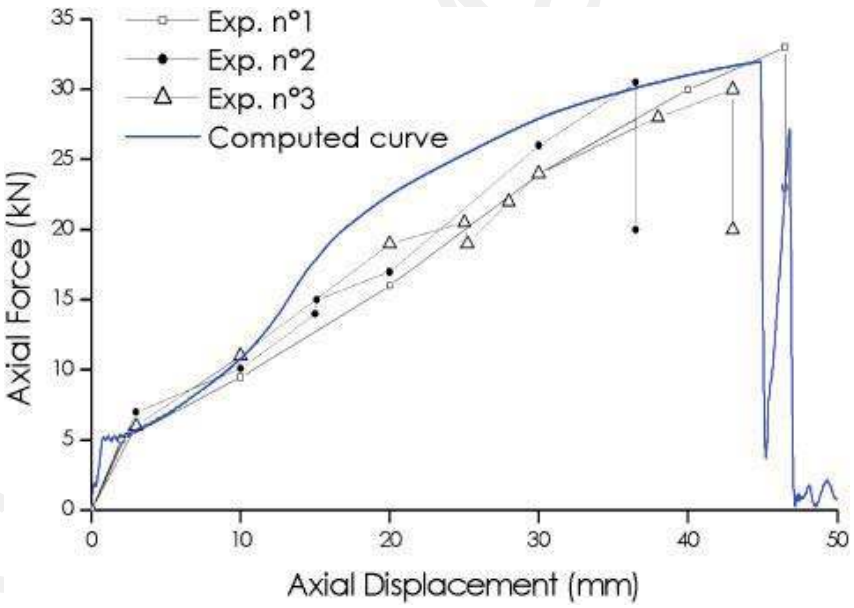

Figure 9. Axial traction force F_a *versus* axial displacement x_a.

2.1.5. Assessment of the robustness of the constitutive model. The ability of the constitutive model developed for the wire netting was investigated by considering further simulations with wire net sheets of different sizes. For this purpose, different wire net sheets, whose mesh size, wire diameter, height, and width have been chosen as reported in Table I, were loaded in the same conditions as those described in Section 2.1.4. For each simulation, the relative error $e_x = (\overline{x}_{comp} - \overline{x}_{exp})/\overline{x}_{exp}$

Table I. Validation stage: geometrical data and relative errors.

Mesh size (cm)	Wire diameter (mm)	Wire net size (mm)		e_x (%)	e_F (%)
		Height	Width		
6–8	2.7	470	960	6	22
8–10	3.0	460	880	8	34
10–12	2.7	390	900	34	16
10–12	3.0	390	900	12	8

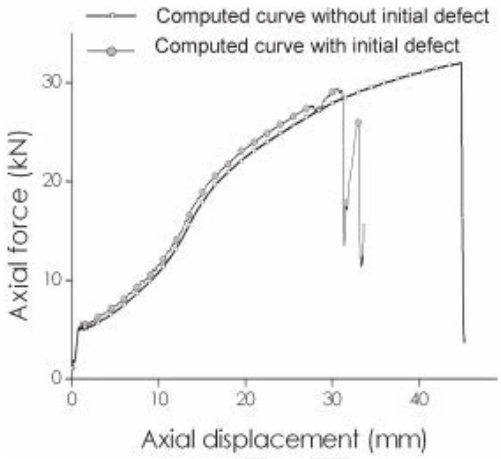

Figure 10. Incidence of the presence of a defect on the response of the sheet.

(resp. $e_F = (\overline{F}_{\text{comp}} - \overline{F}_{\text{exp}})/\overline{F}_{\text{exp}}$) between both computed $\overline{x}_{\text{comp}}$ (resp. $\overline{F}_{\text{comp}}$) and experimental $\overline{x}_{\text{exp}}$ (resp. $\overline{F}_{\text{exp}}$) axial displacement (resp. force) at failure was assessed.

The relative errors presented in Table I remain acceptable, showing that there is rather good agreement between experimental and numerical results. Moreover, the discrepancy observed (relative error larger than 22%) could be attributed to the variability that is likely to exist in material properties of the constitutive wire. Further simulations were run by taking into account random defects within the sheet: a wire was initially equipped with poor mechanical properties prior to simulations. As seen in Figure 10, the incidence of a defect on the response of the sheet is significant and induces a premature failure: both displacement and force at failure are lower that those observed with a defectless sheet. It is worth emphasizing that the shift in the displacement at failure corresponds to a variation on the same order of magnitude as the amplitude of e_x (approximately 30%).

2.2. The filling material

2.2.1. Spatial description. The discrete nature of the filling material, composed of an assembly of limestone rocky particles, makes a discrete approach particularly convenient. Each particle is described by a discrete element. Nevertheless, the particles are far from spherical and have various angular shapes. Given that the shape of these particles greatly influences the interaction mechanisms, it is of paramount importance to realistically account for the particle shapes. Moreover,

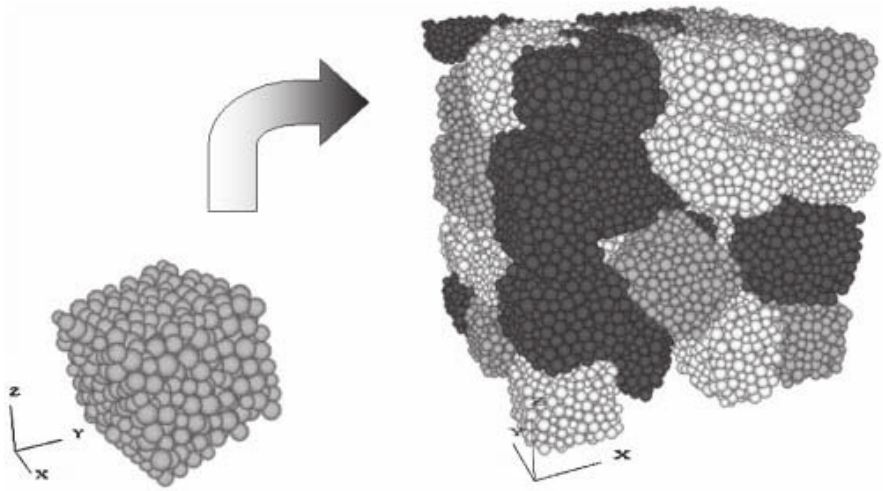

Figure 11. Parallelepiped-like clumps.

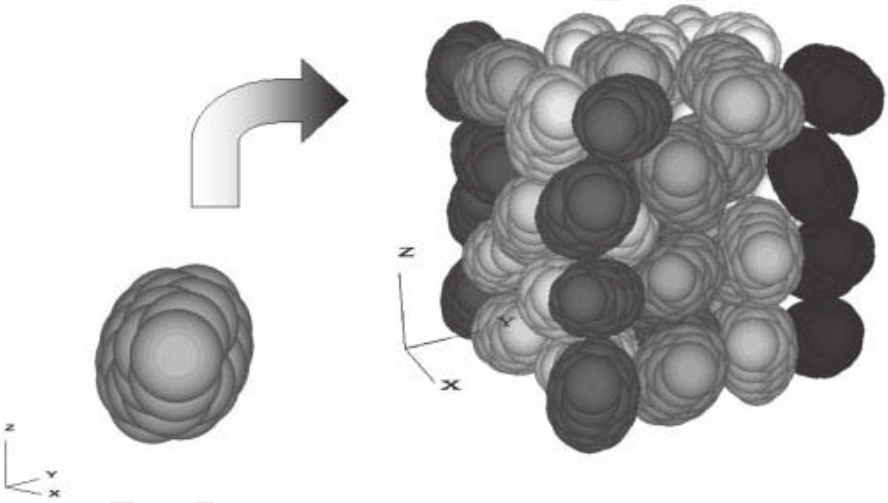

Figure 12. Ellipsoidal clumps.

modelling the wire netting cage and the filling material in the same computational environment has its advantages. PFC^{3D} software is used again to describe the filling material. Basic elements of PFC^{3D} software are spherical but more complex shapes can be described by creating unbreakable agglomerates of spheres (clumps). However, to ensure that simulations can be done within a reasonable duration using standard computers, the number of elements that constitute the clumps should not be too high. In the proposed simulation, clumps are therefore composed of roughly 500 spherical elements, allowing sophisticated shapes to be described, and ensuring that computation time is acceptable. Typically, two types of shapes were created: parallelepiped-like clumps with cut edges (Figure 11) and ellipsoidal clumps (Figure 12).

For parallelepiped-like clumps, the edges of this aggregate of spherical elements are cut out to modify the angularity. The aggregates are calibrated numerically to fulfil with the grain size

requirements of the standard for this specific technique (NFP 94-325-1) [33]. The size of the aggregates placed in the cell follows an empirical statistic Gaussian obtained from experimental grain size distributions [34]. Finally, the aggregates are positioned above the cell and gravity makes them fall into the cell. However, the initial porosity of numerical cells filled only applying gravity is higher than the experimental ones. The experimental average initial porosity is roughly 42%, whereas numerical values are close to 50%. A vibration process of the aggregates reduces the cell porosity by about 5%. Finally, this modelling procedure makes it possible to describe a wide range of assemblies of variously shaped rocky particles, while reproducing the grain size distribution fairly well.

2.2.2. Constitutive modelling. Rocky particles inside a gabion cell interact and a contact zone develops between each pair of adjoining particles. The local behaviour at the contact can be described properly using a contact mechanical model relating both the local normal force F_c^n and the local tangential force F_c^t to both the local normal relative displacement u_c^n and the local tangential relative displacement u_c^t. Many models have been proposed in the literature [35, 36], the simplest one being the elastic–plastic model, which introduces a normal elastic stiffness k_n and a tangential elastic stiffness k_t, both constant, and a local friction angle φ_g. The following local constitutive incremental relations can be inferred:

$$\mathrm{d}F_c^n = k_n \,\mathrm{d}u_c^n \tag{13}$$

$$\mathrm{d}\mathbf{F}_c^t = \min\{\|\mathbf{F}_c^t + k_t \,\mathrm{d}\mathbf{u}_c^t\|, \tan\varphi_g(F_c^n + k_n \,\mathrm{d}u_c^n)\}\frac{\mathbf{F}_c^t + k_t \,\mathrm{d}\mathbf{u}_c^t}{\|\mathbf{F}_c^t + k_t \,\mathrm{d}\mathbf{u}_c^t\|} - \mathbf{F}_c^t \tag{14}$$

Furthermore, granular assemblies are not able to sustain local tensile stress. This is a fundamental feature of this type of material. The following condition is therefore added:

$$F_c^n > 0 \tag{15}$$

However, experimental observations revealed that failures are likely to occur within particles. Superficial failures, responsible for localized damage that only concerns a part of the thin external crown of blocks, coexist with internal failures that break the blocks into two or more parts. The occurrence of these modes depends on the confinement of the blocks. The former mode is encountered under low confinement but under high localized pressures, whereas the latter mode is activated when the adjoining blocks in contact direct a high confinement effect [5, 37, 38]. Moreover, the contact degradation phenomenon is highly dependent on the shape of the blocks near the contact zone [39]. Roughly speaking, these failures can be explained in part by the development of the so-called force chains within the assembly, so that high stresses can be concentrated between particles in contact. Furthermore, it is now well established that a granular medium can be considered as composed of two distinct phases. Specific patterns gathering grains that are joined by contacts transmitting high contact forces may be developed within the granular assembly [40, 41]. Since these patterns are responsible for the ability of the medium to transmit local forces, they are denoted force chains (or solid paths, using the terminology adopted by Horne). These chains constitute the so-called strong phase. In the vicinity of these chains, a network of weak contacts associated with low contact forces exists. Similarly, this network constitutes the so-called weak phase. Force chains transmitting high forces may become unstable if the surrounding weak phase does not ensure a sufficient sustaining effect, a notion that has been supported by several experimental investigations [11, 42, 43]. As suggested by Oda *et al.* [44]. It can therefore be conjectured that the force chains

whose mean direction is close to the major principal direction of the loading may collapse when the stress level along this direction is too high. In some cases, failures occur within elements before collapse. These failures are even more likely to occur when a sustaining effect is ensured by the loading conditions or the shapes of the particles. The lower the number of particles within a gabion, the more probable this is.

As the clumps describing the rocky particles are reputed to be unbreakable, this failure phenomenon, superficial or not, can be taken into account through an elasto-plastic model along the normal direction of contact. The degradation of the material is described by a decrease in the normal contact stiffness. Once the stress limit is reached, the tangent stiffness is zero. The contact stiffness is known to be largely stress dependent and is often described by a parabolic-like law. Here, the decrease in the normal stiffness, induced by the degradation of the materials in the vicinity of the contact area, is modelled by adopting a simple constitutive model that describes the normal behaviour through an elastic–perfectly plastic relation. In these conditions, Equation (13) must be replaced with the following relations:

If $F_c^n < F_{lim}^n$ or if $F_c^n = F_{lim}^n$ and $du_c^n < 0$, then:

$$dF_c^n = k_n \, du_c^n \tag{16}$$

If $F_c^n = F_{lim}^n$ and $du_c^n \geqslant 0$, then:

$$dF_c^n = 0 \tag{17}$$

It is worth noting that the elastic–perfectly plastic relation models the local degradation, which occurs in the vicinity of the contact zone. Attrition phenomena are expected to occur, modifying the shape of contacting particles. This removal of matter is accounted for by reducing the radii of the contacting particles as a function of the plastic component of the normal relative displacement (see Appendix A). This procedure prevents any numerical instability related to the possibly excessive overlapping.

This model is in all likelihood oversimplified with respect to the complex physical phenomena that occur between two rock-like materials in contact. With the aim of developing a computational tool that is manageable for engineering purposes, requiring only a few parameters, it is believed that this approach can be adopted as a first approximation.

2.2.3. Implementation within the PFC^{3D} *environment.* The assembly of clumps, in interaction with the elements describing the wire netting box, is modelled with the PFC^{3D} software. As each wire is described by two nodes located at the two extremities, contacts between clumps and wires are assumed to take place only at those intersection nodes between the wires. This assumption is justified by the size of the clumps, which is greater than the length of the wires. Considering wire coming into contact with clumps at points between the two intersection nodes would considerably complicate the numerical procedure used by PFC^{3D} to model the wires. Introducing intermediate nodes to describe the wires is a possible alternative. Nevertheless, this refinement would be very time consuming, and the gain in precision would be counter balanced by a longer computation time.

First, the wire netting box is created from a single plane wire net sheet. The sheet is folded along the edges to constitute the box, once the six faces are joined up (Figure 13).

Then, as indicated in Section 2.2.1, the clumps that describe the filling material are placed in the box by gravity-driven deposition, as done in practice with real gabion cells.

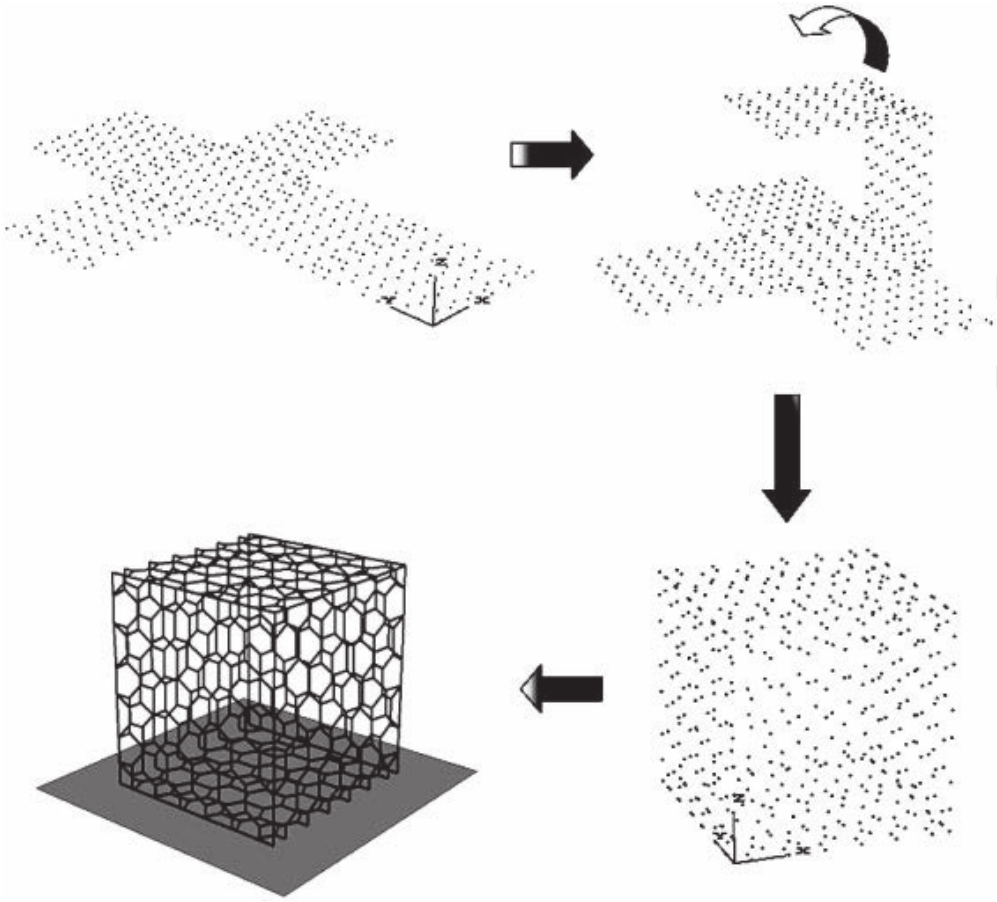

Figure 13. Numerical fabrication of the wire netting box.

PFC^{3D} is based on the soft contact approach that allows overlapping to occur at contact points [27]. This contact model easily integrates constitutive relations given in Equations (14)–(17). Once a clump and an element of the wire netting box overlap together, a contact force develops between these two bodies. This force, computed from the constitutive relations (14)–(17), induces the displacement of the element, leading to the deformation of the wire cage. The resulting contact force contributes to the reaction force applied by the wire cage to the filling material, thereby ensuring a confining effect. Finally, using PFC^{3D}, the displacement of any element (or clump) is computed over time, so that the deformation of the whole cell as well as the different forces acting between the clumps and the wires of the box can be analysed.

2.3. Numerical simulation of the response of a single cell

2.3.1. Calibration stage along confined loading paths. The model developed throughout this paper is attractive because it requires that only a few microscopic (namely, on contact scale) parameters be calibrated, namely both elastic normal k_n and tangential k_t stiffness, the friction angle φ_g and the limit normal force F_{lim}^n. This is of course more advantageous than phenomenological approaches, which generally introduce a large number of parameters.

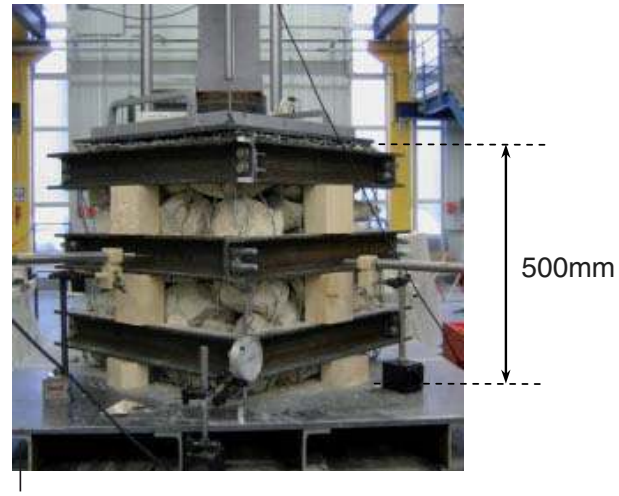

(a)

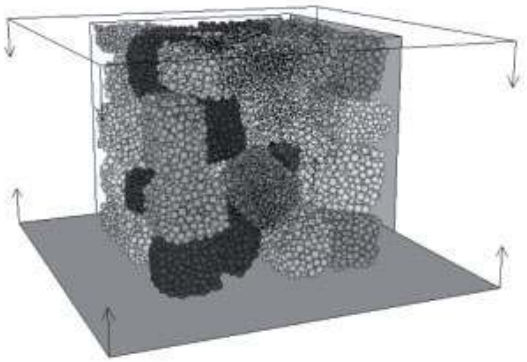

(b)

Figure 14. Confined compressive tests. Experimental apparatus (a) and numerical model (b).

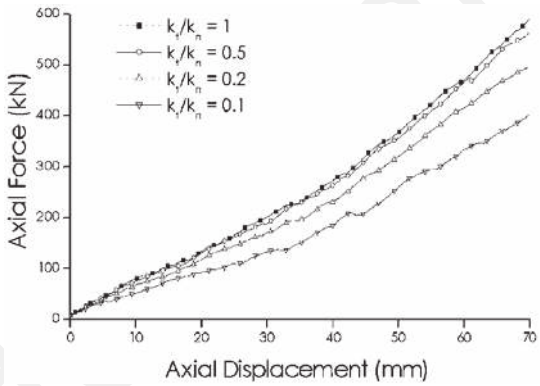

Figure 15. Influence of the ratio $\alpha = k_t/k_n$ for confined compression conditions.

The purpose of this section is to calibrate these material parameters based on the comparison between experimental data and the results obtained from numerical simulations. Experimental tests were carried out on cubic cells 500 mm in height [45]. The wire net was made of 2.7-mm-diameter cable; the filling material was composed of limestone angular blocks, whose grain size distribution was uniform within the range [80–180 mm] and whose density is chosen equal to 2640 kg/m^3. The porosity of the samples ranged from 42 to 43%. During the test, the four lateral sides were blocked and an axial compressive displacement at a constant rate of 5 mm/min was imposed on the upper side (Figure 14(a)). Forces applied to the upper side were recorded in terms of axial displacement. Several experimental tests (denoted C tests) were conducted to assess the repeatability of the test. Two tests are considered herein: the samples used in experimental tests C1 and C2 were characterized by a porosity of 42.7 and 42.6%, respectively. As shown in Figure 15, a slight shift can be noted between the two experimental curves. This shift stems from the difference in the fabric of the two initial experimental samples. Even if the porosity was more or less the same for

the two samples, the geometrical arrangement of the clumps inside the cell was different. This is a classical result that has been thoroughly described for discrete materials [10, 46, 47]. This phenomenon was all the more pronounced for clump assemblies considered herein because the number of clumps was not very high.

This oedometric loading path was simulated using parallelepiped-like clumps (Figure 14(b)). The experimental loading procedure was reproduced by imposing lateral displacements equal to the zero value; the force applied to the upper side was recorded in terms of the axial displacement. As a first approximation, the wire netting was not taken into account. During such tests, the vertical parts of the wire netting are loaded in compression, which is likely to induce bending strains in the wires. However, the global rigidity of the entire cell in the axial direction (which implies rocky particle stiffness) is much larger than the bending rigidity of the wires. This is necessary because, in confined conditions, the wire netting is assumed not to play a great mechanical role in the cell response. The main advantage of considering only the filling material is that the computation time of the simulations is reduced, without altering the quality of the results.

During the simulations, the friction coefficient ($\tan\varphi_g$) was chosen equal to 0.5 ($\varphi_g = 27°$). This value corresponds to the average value commonly reported for limestone [36]. In the absence of specific experimental investigations, this value was adopted. It must be noted that the initial porosity of the numerical specimen is slightly greater than that of the tested samples (43.6% instead 42.6 and 42.7%). As the macroscopic behaviour of an assembly of contacting particles with rough surfaces depends to a large extent on the local behaviour at contact points, a parametric analysis was done to assess the influence of the ratio $\alpha = k_t/k_n$. It was established from numerical simulations that the influence of this ratio is negligible if $\alpha \in [0.2; 1]$. As shown in Figure 15, the curves giving the evolution of the resulting axial force in terms of axial displacement are fairly close if $k_t/k_n > 0.2$. In what follows, confined compression is simulated using $\alpha = 1$.

The normal elastic stiffness can be assessed from the Young modulus E_l of limestone; if we assume that the contact area is circular with a radius r_l, then we have:

$$k_n \approx \frac{E\pi r_l^2}{h} \tag{18}$$

where h is the characteristic size of the element considered. $E_l = 58\,000$ MPa is a current value reported in data tables [36]; if we assume that $h \approx 100$ mm and that a reasonable value of r_l is approximately 2% of h, then it follows that $k_n \approx 7.3$ MN/m.

The comparison between experimental and numerical curves shows that a satisfying fit of the experimental data is obtained with high values of normal elastic stiffness k_n and tangential elastic stiffness k_t (Figure 16): typically, $k_n = k_t = 10$ MN/m, which is on the same order of magnitude as the value 7.3 MN/m. This calibration was performed with $F_{lim} = 2500$ N. Thus, in the following, simulations will be carried out by using the parameters reported in Table II.

As depicted in Figure 16, the evolution of the axial force is nonlinear with respect to the axial displacement: the greater the axial displacement, the greater the curve's slope, which means that the axial stiffness of the material increases with axial displacement. In these conditions, first the axial compression of the sample is linked to the rearrangement of the clumps by sliding and rolling. This phase is very brief. Because of the reduction in cell volume, rearranging the clumps becomes more difficult; the predominant mechanism is the normal compression at contact between clumps, inducing a significant increase in the overall stiffness of the cell.

The ability of the model to predict the response of a cell in dynamical loading conditions is the subject of analysis in the next section.

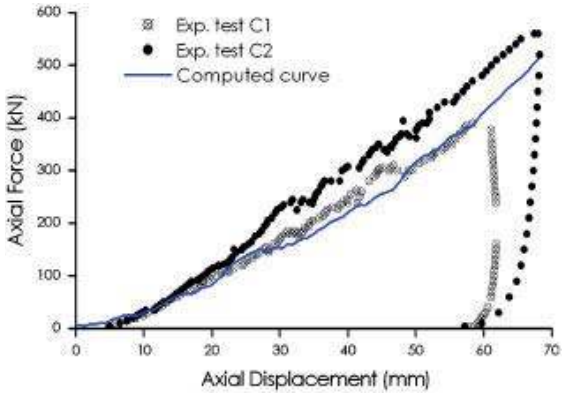

Figure 16. Confined compression tests. Comparison between experimental and numerical results using an elastic–perfectly-plastic relation in the normal direction.

Table II. Filling material: calibration of the parameters.

k_n (MN/m)	k_t (MN/m)	$\tan\varphi_g$	F_{lim} (N)
10	10	0.5	2500

2.3.2. Validation stage from impact tests. In order to assess the capability of the cell model, impact tests were simulated, and subsequent results were compared with those obtained during an experimental testing campaign. Experimental tests impacted a gabion cell placed on a rigid concrete platform using a sphere equipped with an accelerometer (Figure 17) [48]. The four lateral sides of the gabion cell were free to move (unconfined conditions) or were blocked (confined conditions). The mass of the sphere was 250 kg, with a radius of 540 mm; different impact velocities were considered. Cube-like cells were used with a 500-mm-long edge. The porosity of the cells ranged from 39 to 43%. During each impact, the acceleration of the sphere was recorded over time, yielding the reaction force exerted by the cell onto the sphere by applying Newton's law. Then, the change in the reaction force applied by the cell to the boulder can be investigated over the dimensionless ratio δ/a, where δ is the penetration depth of the boulder into the cell and a is the height of the cell.

These tests were simulated using parallelepiped clumps with a density of 2640 kg/m^3. The filling material was created by respecting the grain size distribution used for experimental tests. The deposition process of clumps inside the cell has made it possible to make different initial arrangements with a single porosity of approximately 43.6%. Parameters related to the filling material used for the simulations are those previously indicated in Table II, and those associated with the wire netting box are reported in Table III. In order to assess the influence of the initial arrangement of clumps within the cell, several simulations were performed with different initial arrangements. The experimental loading procedure was reproduced and the reaction force applied to the sphere was computed over time. Experimental and numerical simulations were carried out with an initial velocity of the sphere before impact of 8 m/s, which corresponds to an initial kinetic energy of 8 kJ. The results obtained in both confined and unconfined conditions are presented in

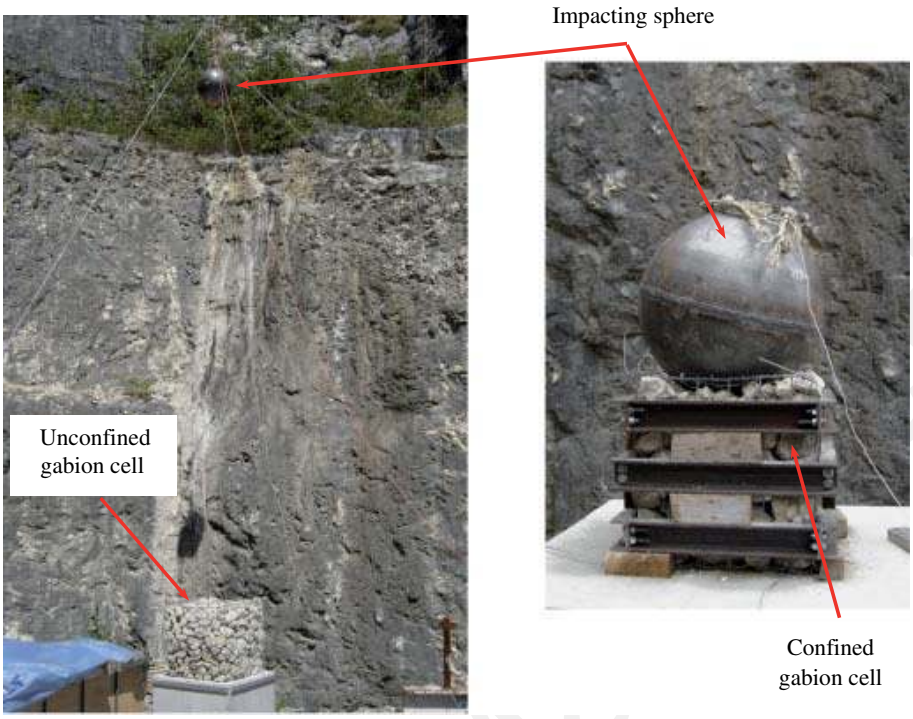

Figure 17. Experimental impact tests on confined and unconfined gabion cells.

Table III. Gabion cell: geometrical and numerical parameters used for the simulations.

Mesh size (cm)	Wire diameter (mm)	λ_ε	λ_k
8–10	2.7	0.4	0.66

Figures 18 and 19. As expected, the response of the cell depends on the initial arrangement. Thus, for both confined and unconfined conditions, an average curve was plotted. This curve falls within a band delimited by a lower curve and a upper curve indicating the standard deviation around the average curve. Namely, at each value of the ratio δ/a, the upper (resp. lower) curve is built from the average curve by operating an upward (resp. downward) shift equal to the standard deviation related to the reaction force obtained for the considered value of δ/a. The comparison between experimental and numerical results, shown in Figures 18 and 19, tends to prove that the general trends of the changes in the reaction force exerted to the sphere as a function of the axial displacement of the sphere are correctly reproduced by the numerical model. In both cases, the numerical results closely match experimental data that fall within the band delimited by the standard deviation curves. In particular, the numerical curves, like the experimental curves, reveal that the increase in the reaction force exerted on the sphere is much stronger in confined conditions, and that the maximum reaction force reached is higher in confined conditions for identical impact conditions. In addition, the reaction force continuously increases with the penetration depth of the boulder in confined conditions, whereas in unconfined conditions the curve giving the evolution of

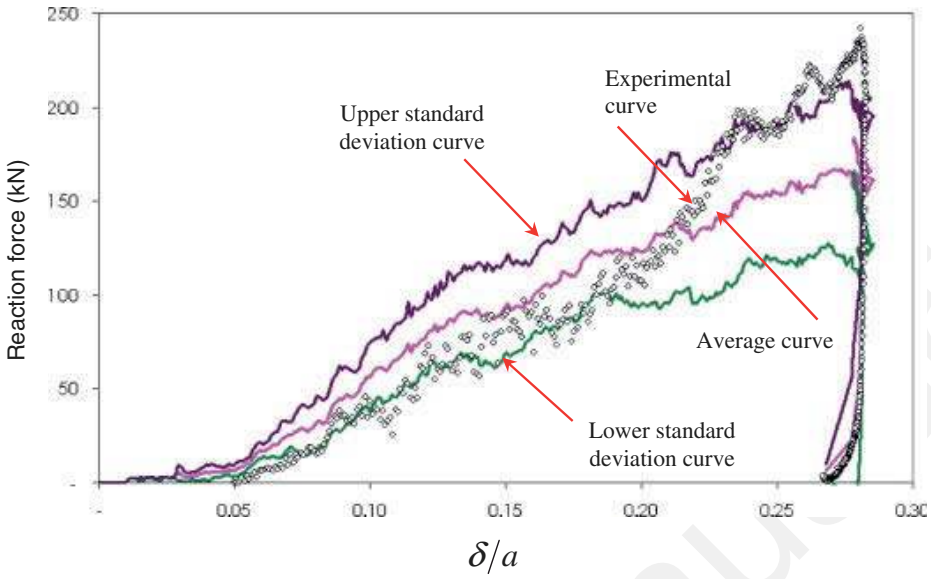

Figure 18. Impact tests in confined conditions: comparison of experimental and numerical results.

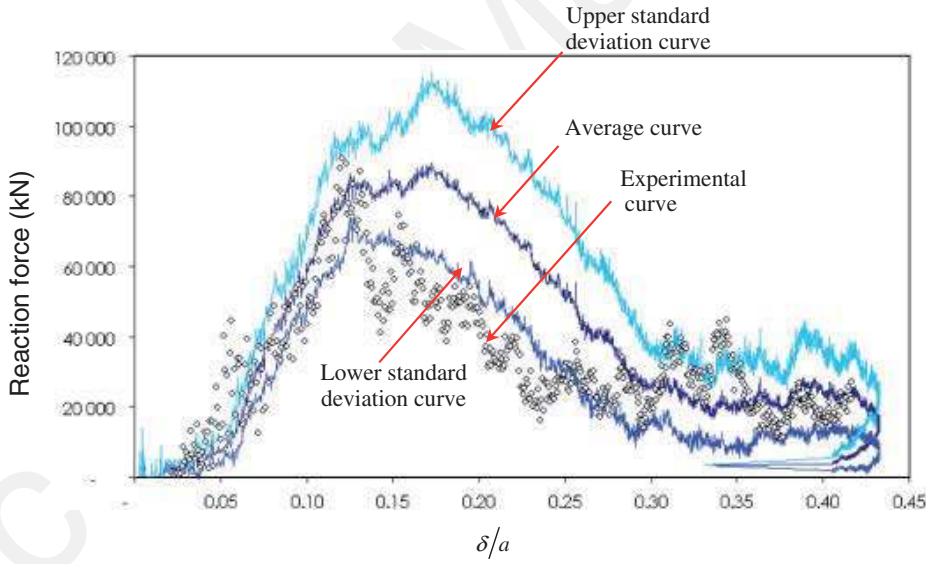

Figure 19. Impact tests in unconfined conditions: comparison of experimental and numerical results.

the reaction force passes through a maximum, then significantly decreases until a small residual value.

These first elements of validation are particularly encouraging, confirming the relevance of the proposed approach based on a discrete description of both the wire netting box and the filling material.

3. MECHANICAL MODELLING OF A CELLULAR STRUCTURE

This section analyses a cellular structure composed of an assembly of several identical cubic cells, arranged following a regular array. Using a multiscale approach, a computational tool is developed by taking into account the cell model presented in Section 2. The discrete nature of the structure, whose cells can be regarded as the elementary parts, was once again justified using a simulation based on a discrete element method. In particular, large strains that are likely to occur within the structure, directed by a discontinuous displacement field of the cells, can be accounted for by a discrete element method in a very natural and straightforward manner. In addition, this choice, rather than a continuous alternative method such as a finite element method, makes it possible to develop a computational tool in the PFC^{3D} environment, which ensures that all computational developments are made in the same environment, a valuable feature.

3.1. Spatial description

The structure is assumed to be set up on a perfectly plane, horizontal soil, just below a slope assimilated to an inclined plane (Π) (Figure 20). The direct triad $\{\mathbf{x}, \mathbf{y}, \mathbf{z}\}$ is defined as follows:

$\mathbf{z}$ is the upward vertical direction;
$\mathbf{y}$ is the horizontal direction of plane (Π);
$\mathbf{x} = \mathbf{y} \wedge \mathbf{z}$.

Cubic cells are initially disposed periodically in such a way that the centres of cells belong to parallel, regularly spaced vertical planes (Figure 22). The lateral faces of the cells are placed parallel to both the $\mathbf{x}$-direction and $\mathbf{y}$-direction. The distance between two vertical contiguous planes is equal to the edge of the cells, denoted a. In a given vertical plane, the cells are disposed row by row, and a shift s_x is introduced along the $\mathbf{x}$-direction between two successive rows. The cells of two contiguous vertical planes are in contact two by two, with no shift along the

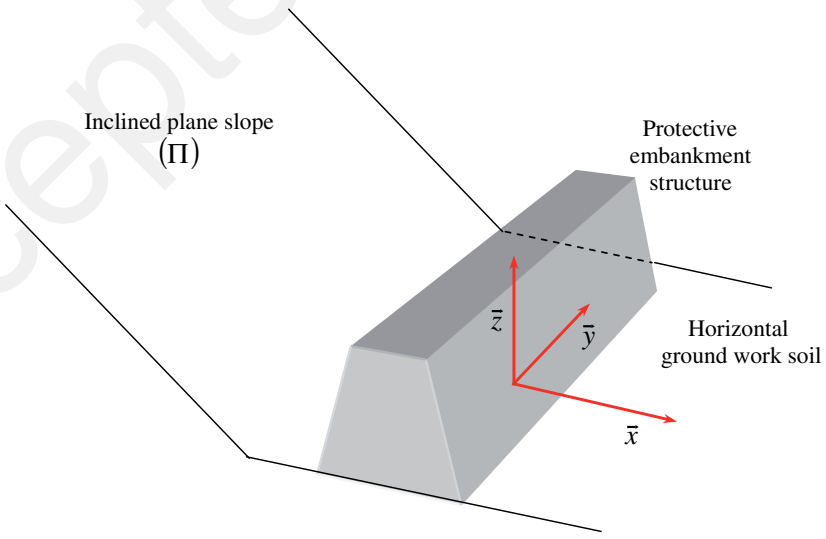

Figure 20. Local topological configuration and reference frame.

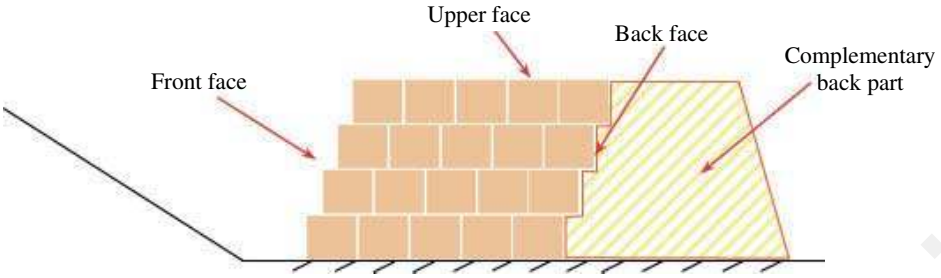

Figure 21. Technological scheme and wordlist of a cellular structure.

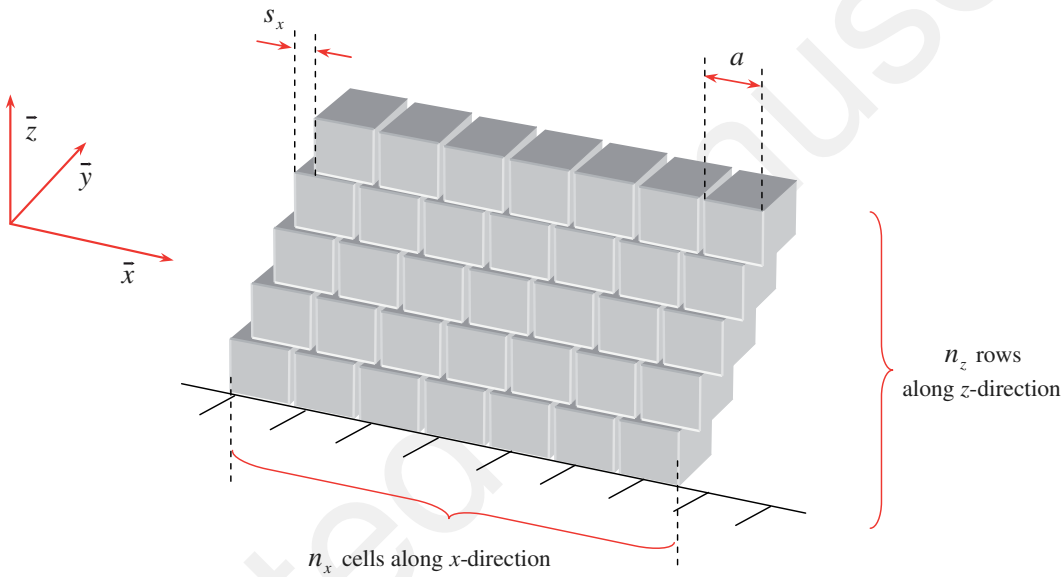

Figure 22. Initial arrangement of cells in the parallel vertical planes.

x-direction (Figure 23). Thus, the centres of cells also belong to successive horizontal planes. Considering a given horizontal plane of equation $z = z_0$, the number of cells along the **x**-direction is denoted $n_x(z)$ and the number of cells along the **y**-direction is denoted $n_y(z)$. In what follows, for the sake of simplicity, n_x and n_y are assumed not to depend on z, as in Figures 21–24. Likewise, the number of cells n_z along the **z**-direction, in any vertical plane, is constant (Figure 24). The front, upper, and lateral faces are assumed to be free. The lower cells lie directly on the soil, with no additional anchorage. Likewise, adjoining cells are initially placed in contact, with no fixation system. The boundary condition applied to the back face models the specific complementary structural element constituting the back part of the structure (possibly including a kernel structural element) (Figure 21). In absence of such complementary structural elements, the back face is reputed free. On the contrary, in the case of a sufficiently rigid complementary part, the displacements of the back face will be nil. Generally, the technological solutions adopted require modelling this boundary condition, at a given point of the back face, using a constitutive

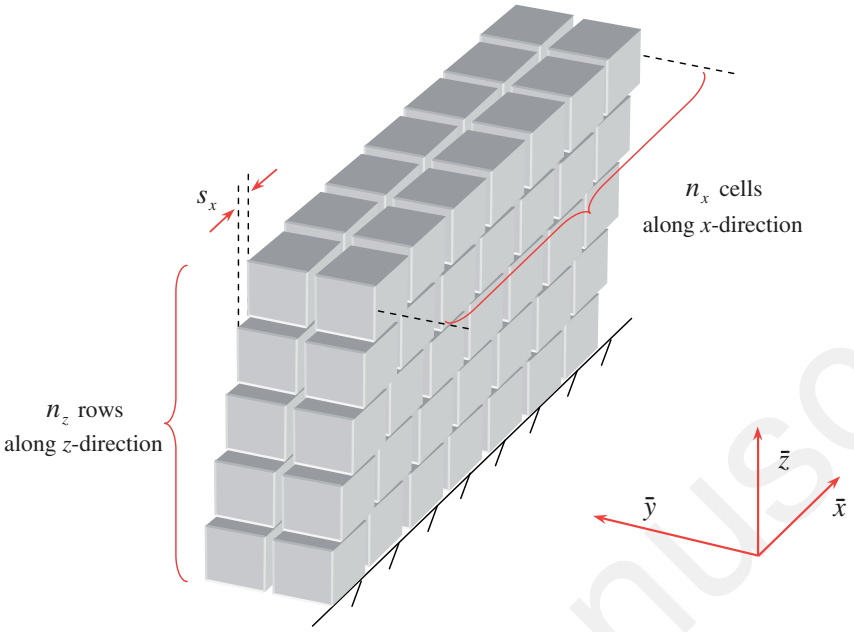

Figure 23. Initial disposition of cells between two successive parallel vertical planes.

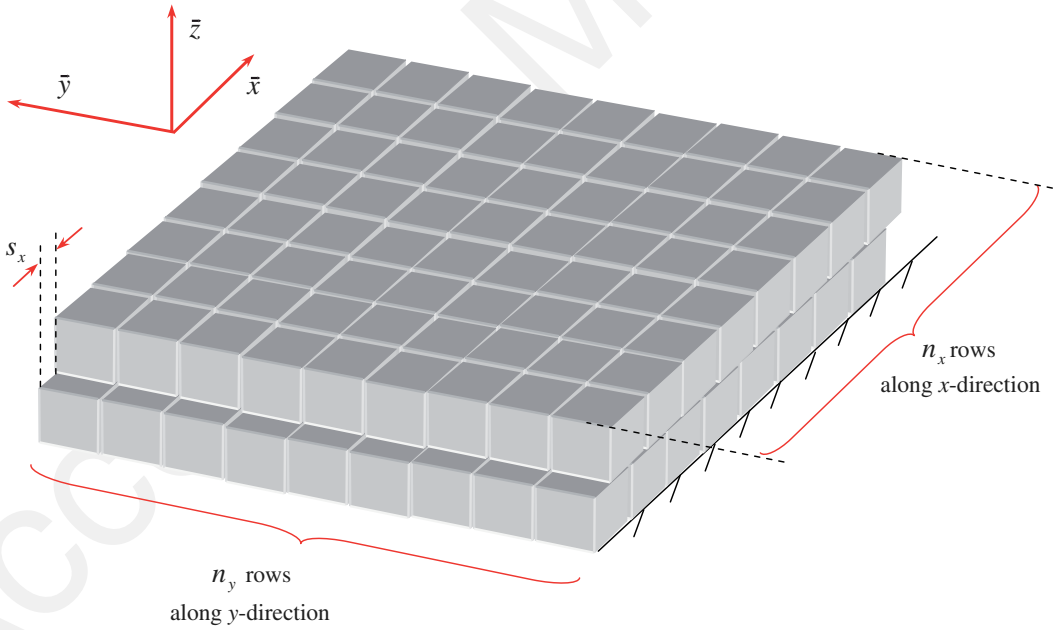

Figure 24. Initial arrangement of cells in the horizontal planes.

relation expressing the stress vector exerted by the complementary back structure in terms of the displacement of this point. Hereafter, as a simple and pedagogic illustration, the back face will be reputed free.

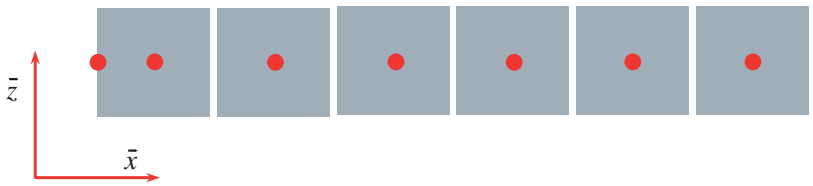

Figure 25. Nodal description of cells. A single node is affected for each cell, and an additional node is required for the first cell placed at the upstream extremity.

Let each cell be assimilated to a material point in the sense of continuum mechanics. Thus, a homogeneous displacement field exists within each cell. By considering that the incident boulder has a trajectory, just before the impact, nearly parallel to the **x**-direction without any spin velocity, it will be assumed, at least as a first approximation, that the displacement field within each cell has a single component along the **x**-direction. The strain field within each cell therefore takes the following straightforward form:

$$\bar{\bar{\varepsilon}} = \begin{bmatrix} \varepsilon_{xx} & 0 & 0 \\ 0 & 0 & 0 \\ 0 & 0 & 0 \end{bmatrix} \tag{19}$$

Thus, no shearing takes place within cells, and no strain occurs along the **y**-direction or the **z**-direction. As a consequence, each cell is loaded along an oedometric path. That seems reasonable for lower cells, since upper and lateral cells induce a confinement that can prevent (at least partly) strains along lateral and vertical directions from developing. This is certainly more questionable for upper cells. However, this approximation will be adopted in the sequel.

As a direct consequence of Equation (19), the changes in the strain state of a given cell are perfectly described by following the displacement of two points of the cell over time. As the n_x adjoining cells of a given row along the **x**-direction remain in contact, $n_x - 1$ complementary kinematic relations exist, so that $n_x + 1$ nodes are sufficient to describe the kinematics of the n_x adjoining cells. n_x nodes can be located at the centres of the n_x cells; a complementary node is added on the upstream face of the row's first cell (Figure 25). Thus, in the continuity of the previous discrete modelling, the actual structure is replaced with a mesh of nodes. Interaction forces, which take into account the constitutive behaviour of cells, exist between adjoining nodes.

3.2. Constitutive modelling

3.2.1. Definition of forces acting on a cell. Let a given cell 'i' of the structure be considered. In the most general case, once relative displacements between cells have taken place, the cell 'i' is neighboured by 10 adjoining cells 'i_k', with $k = 1, \ldots, 10$, as illustrated in Figure 26. The purpose of this section is to model the interaction force that exists between the corresponding nodes 'i' and 'i_k', as a function of their relative positions.

The resultant forces $\mathbf{F}_{i_k,i}$ exerted by the adjoining cells 'i_k' onto the cell 'i' have two different origins. The first is related to the constitutive behaviour of cells along an oedometric loading path, directing axial forces $F^{\mathrm{n}}_{i_3,i}$ and $F^{\mathrm{n}}_{i_6,i}$ oriented along the **x**-direction, together with lateral forces $F^{\mathrm{n}}_{i_1,i}$, $F^{\mathrm{n}}_{i_2,i}$ and $F^{\mathrm{n}}_{i_4,i}$, $F^{\mathrm{n}}_{i_5,i}$ oriented along the **y**-direction, and $F^{\mathrm{n}}_{i_7,i}$, $F^{\mathrm{n}}_{i_8,i}$ and $F^{\mathrm{n}}_{i_9,i}$, $F^{\mathrm{n}}_{i_{10},i}$ oriented

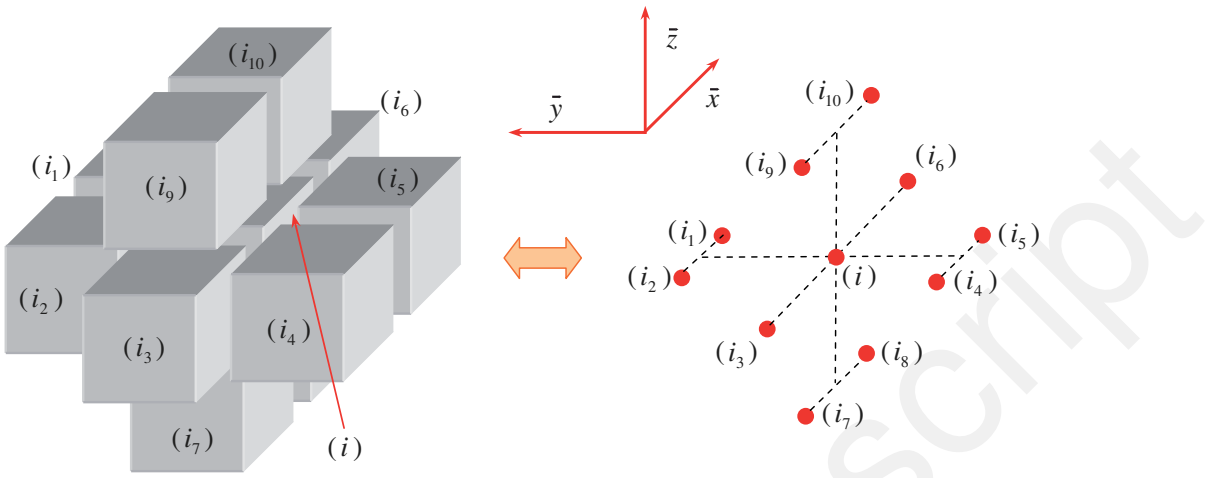

Figure 26. Arrangements between adjoining cells and corresponding nodes (after relative displacements have occurred).

along the **z**-direction. As seen in Section 2.3.1, lateral forces stem from the confinement imposed on the lateral sides of cell 'i'. The second origin is linked to the relative displacement that is likely to occur between adjoining cells that belong to two different rows aligned along the **x**-direction. As the strain of cell 'i' induces normal forces between cells 'i' and 'i_1', 'i_2', 'i_4', 'i_5', 'i_7', 'i_8', 'i_9', and 'i_{10}', friction can be mobilized yielding to the development of tangential forces $F^{\mathrm{t}}_{i,k}$. To illustrate, let us consider the adjoining cells 'i' and 'i_1'. Cell 'i_1' applies a normal force $F^{\mathrm{n}}_{i_1,i}$ onto cell 'i'. Likewise, since cell 'i_1' strains in confinement conditions, cell 'i' directs a normal force F^{n}_{i,i_1} on cell 'i_1'. As the displacement of cells along the **y**-direction is not taken into account by the proposed simulation, an out-of-equilibrium state can persist along this direction, preventing forces $F^{\mathrm{n}}_{i_1,i}$ and F^{n}_{i,i_1} from being equal. Thus, the tangential force $F^{\mathrm{t}}_{i_1,i}$ between cells 'i' and 'i_1' can be defined from the standard Coulomb law by considering the average normal force $\overline{F}^{\mathrm{n}}_{i_1,i} = \frac{1}{2}(F^{\mathrm{n}}_{i_1,i} + F^{\mathrm{n}}_{i,i_1})$:

$$F^{\mathrm{t}}_{i_1,i} = \mu_{\mathrm{c}} \overline{F}^{\mathrm{n}}_{i_1,i} \tag{20}$$

where μ_{c} denotes the friction coefficient between adjoining cells. It must be noted that $F^{\mathrm{t}}_{i_1,i}$ is nil if the relative velocity between the two adjoining cells is nil. The same reasoning can be extended to other adjoining cells.

3.2.2. Calculation of forces acting on a cell. Calculation of normal forces $F^{\mathrm{n}}_{i_k,i}$ is now the subject of interest. As cells are loaded in oedometric conditions, the results obtained from numerical investigations presented in Section 2.3.1 can be used. Given a cell 'i', compressed along the **x**-direction, an axial stress σ^{a}_i develops on the two faces normal to **x**. The evolution of this stress is a function of the evolution of the axial strain $\varepsilon^{\mathrm{a}}_i$ within the cell. Likewise, a lateral stress σ^{l}_i develops on the four faces normal to **y** or **z**. The evolution of this stress depends on the evolution of the axial stress σ^{a}_i within the cell. As shown in Figure 27(b), a hysteretic evolution of the lateral stress exists over a closed axial stress cycle. In the following, this hysteretic behaviour will be omitted, so that the dependency of $\mathrm{d}\sigma^{\mathrm{l}}_i$ upon $\mathrm{d}\sigma^{\mathrm{a}}_i$ is described by a reversible linear relation.

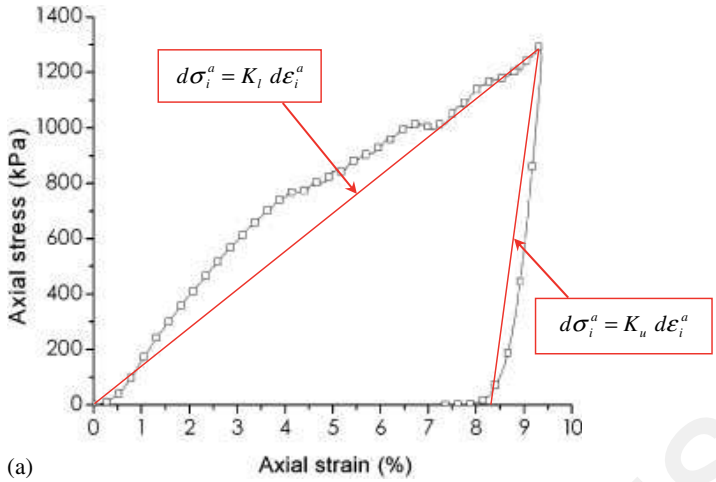

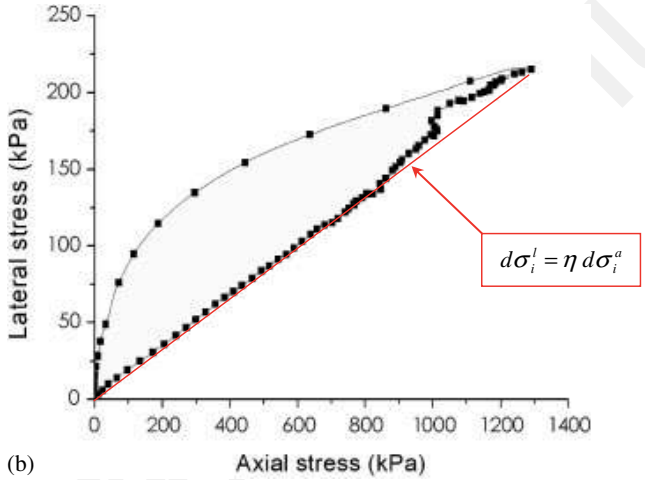

Figure 27. Calibration of a bilinear model along a confined compressive loading path: (a) axial stress evolution and (b) lateral stress evolution.

Finally, a simple bilinear model can be adopted (Figure 27(a) and (b)):

$$\text{If } \mathrm{d}\varepsilon_i^{\mathrm{a}} \geqslant 0 \text{ (loading condition), then } \mathrm{d}\sigma_i^{\mathrm{a}} = K_{\mathrm{l}}\mathrm{d}\varepsilon_i^{\mathrm{a}} \tag{21}$$

$$\text{If } \mathrm{d}\varepsilon_i^{\mathrm{a}} < 0 \text{ (unloading condition), then } \mathrm{d}\sigma_i^{\mathrm{a}} = K_{\mathrm{u}}\mathrm{d}\varepsilon_i^{\mathrm{a}} \tag{22}$$

$$\mathrm{d}\sigma_i^{\mathrm{l}} = \eta \mathrm{d}\sigma_i^{\mathrm{a}} \tag{23}$$

where the values of coefficients K_1, K_u and η obtained after calibration are reported in Table IV.

The normal forces applied by cell 'i_k' to cell 'i' can be assessed from both axial stress and lateral stress as follows:

$$F_{i_k,i}^{\mathrm{n}} = S_{i,i_k}\sigma_{i_k}^{\mathrm{a}} \quad \text{or} \quad F_{i_k,i}^{\mathrm{n}} = S_{i,i_k}\sigma_{i_k}^{\mathrm{l}} \tag{24}$$

where S_{i,i_k} is the area of the contact surface between cells 'i' and 'i_k'.

Table IV. Constitutive parameters for the cell along the oedometric path.

K_1 (kPa)	K_u (MPa)	η
6667	60,000	0.163

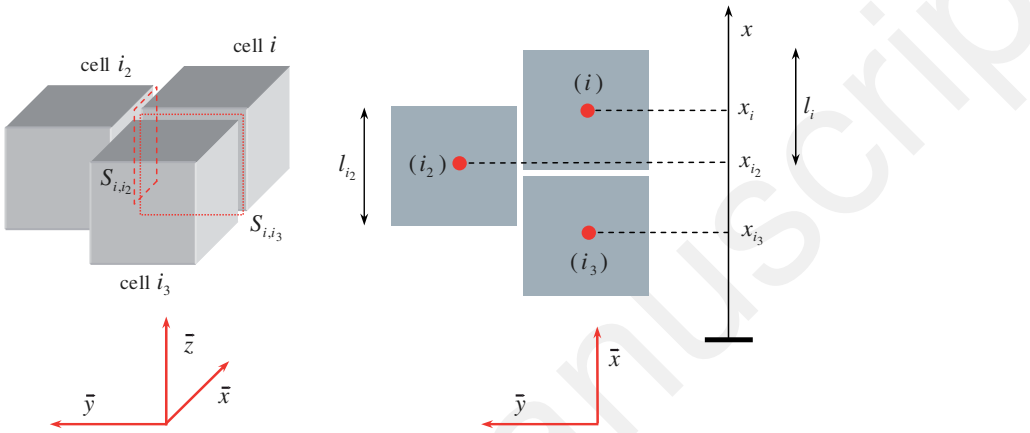

Figure 28. Definition of the contact surface between adjoining cells.

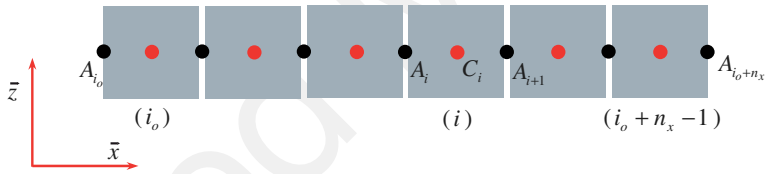

Figure 29. Designation of adjoining cells in a row.

If $k \in \{3, 6\}$, then $S_{i,i_k} = a^2$.

If $k \in \{1, 2, 4, 5, 7, 8, 9, 10\}$, then $S_{i,i_k} = a|x_i + l_i/2 - (x_{i_k} - l_{i_k}/2)|$ where l_i is the current width of cell 'i' along the **x**-direction, and x_i is the current position of the corresponding node 'i' along the **x**-direction (Figure 28).

The calculation of the axial (resp. lateral) stress σ_i^{a} (resp. σ_i^{l}) using constitutive relations (21)–(23) requires that strain $\varepsilon_i^{\mathrm{a}}$ be determined. For this purpose, let a row of n_x contiguous cells along the **x**-direction be considered, from cell 'i_0' to cell '$i_0 + n_x - 1$' (Figure 29). Point C_i corresponds to the node associated with a given cell 'i', and point A_i is located at the interface between the two contiguous cells '$i - 1$' and 'i'. A_{i_0} corresponds to the complementary node associated with the first cell of the row. Hereafter, this node will be referred to as the frontal node.

Denoting x_i^A (resp. x_i^C) the abscissa of point A_i (resp. C_i), it follows that:

$$x_i^C = \frac{x_i^A + x_{i+1}^A}{2} \tag{25}$$

Introducing the quantities $\Delta x_i^A = x_i^A - x_{i-1}^A$ and $\Delta x_i^C = x_i^C - x_{i-1}^C$, for $i \in \{i_0 + 1, \ldots, i_0 + n_x\}$, Equation (25) implies that:

$$\Delta x_i^A + \Delta x_{i+1}^A = 2\Delta x_i^C \tag{26}$$

Finally, Δx_{i+1}^A can be deduced from the recursive expression given in Equation (26):

$$l_i = \Delta x_{i+1}^A = 2(x_{i_0}^C - x_{i_0}^A) + 2 \sum_{k=i_0+1}^{i} (-1)^{k-i_0} \Delta x_k^C \tag{27}$$

As $\varepsilon_i^{\mathrm{a}} = \frac{a - l_i}{a}$, it follows that:

$$\varepsilon_i^{\mathrm{a}} = \frac{1 - 2(x_{i_0}^C - x_{i_0}^A)}{a} - 2 \sum_{k=i_0+1}^{i} (-1)^{k-i_0} \frac{\Delta x_k^C}{a} \tag{28}$$

Thus, for a given configuration of cells belonging to a given row oriented along the **x**-direction and defined by the abscissa x_k^C and $x_{i_0}^A$, the axial strain $\varepsilon_i^{\mathrm{a}}$ within any cell 'i' can be computed.

3.3. Boundary conditions

The structure has a roughly parallelepiped shape, and thus appropriate boundary conditions have to be adjoined on the six boundary sides. The back side, the two lateral sides and the upper surface of the structure are assumed to be free, which means that no external stress is applied to the nodes related to these surfaces. The frontal surface is reputed free before the boulder impacts the structure; once an impact occurs, the boundary condition on the frontal surface is defined by the penetration of the boulder.

3.3.1. Modelling the impact. During the impact, the boulder, modelled by a rigid sphere of centre G, penetrates into one or several frontal cells. When the boulder penetrates into a frontal cell whose frontal node is A_{i_0}, it is assumed, if $\mathrm{d}x_G > 0$, that the incremental displacements $\mathrm{d}x_G$ and $\mathrm{d}x_{i_0}^A$ of nodes G and A_{i_0} over time increment $\mathrm{d}t$ are linked by the relation:

$$\mathrm{d}x_{i_0}^A = \mathrm{d}x_G \tag{29}$$

Equation (29) makes it possible to compute the position of the frontal node of any cell in interaction with the boulder. By assuming that impacted cells are loaded in confined conditions, the reaction force $F_{i_0}^G$ applied by the cell 'i_0' to the boulder can be assessed from the numerical simulation of impact tests developed in Section 2.3.2. For a given boulder's initial kinetic energy, the following simple bilinear model, which gives the evolution of the reaction force $F_{i_0}^G$ applied to the boulder in terms of the dimensionless penetration depth $\varepsilon_{i_0}^{\mathrm{a}} = \delta/a$, can therefore be proposed (Figure 30a):

$$\text{If } \mathrm{d}\varepsilon_{i_0}^{\mathrm{a}} \geqslant 0 \text{ (loading condition), then } \mathrm{d}F_{i_0}^G = K_{\mathrm{imp}}^{\mathrm{l}} a^2 \, \mathrm{d}\varepsilon_{i_0}^{\mathrm{a}} \tag{30}$$

$$\text{If } \mathrm{d}\varepsilon_{i_0}^{\mathrm{a}} < 0 \text{ (unloading condition), then } \mathrm{d}F_{i_0}^G = K_{\mathrm{imp}}^{\mathrm{u}} a^2 \, \mathrm{d}\varepsilon_{i_0}^{\mathrm{a}} \tag{31}$$

where $\varepsilon_i^{\mathrm{a}}$ is defined by the ratio of the penetration depth δ of the boulder into the impacted cell to the height a of the impacted cell. In order to appreciate the influence of the boulder's initial kinetic energy on the evolution of $F_{i_0}^G$ in terms of $\varepsilon_i^{\mathrm{a}}$, three further numerical simulations were

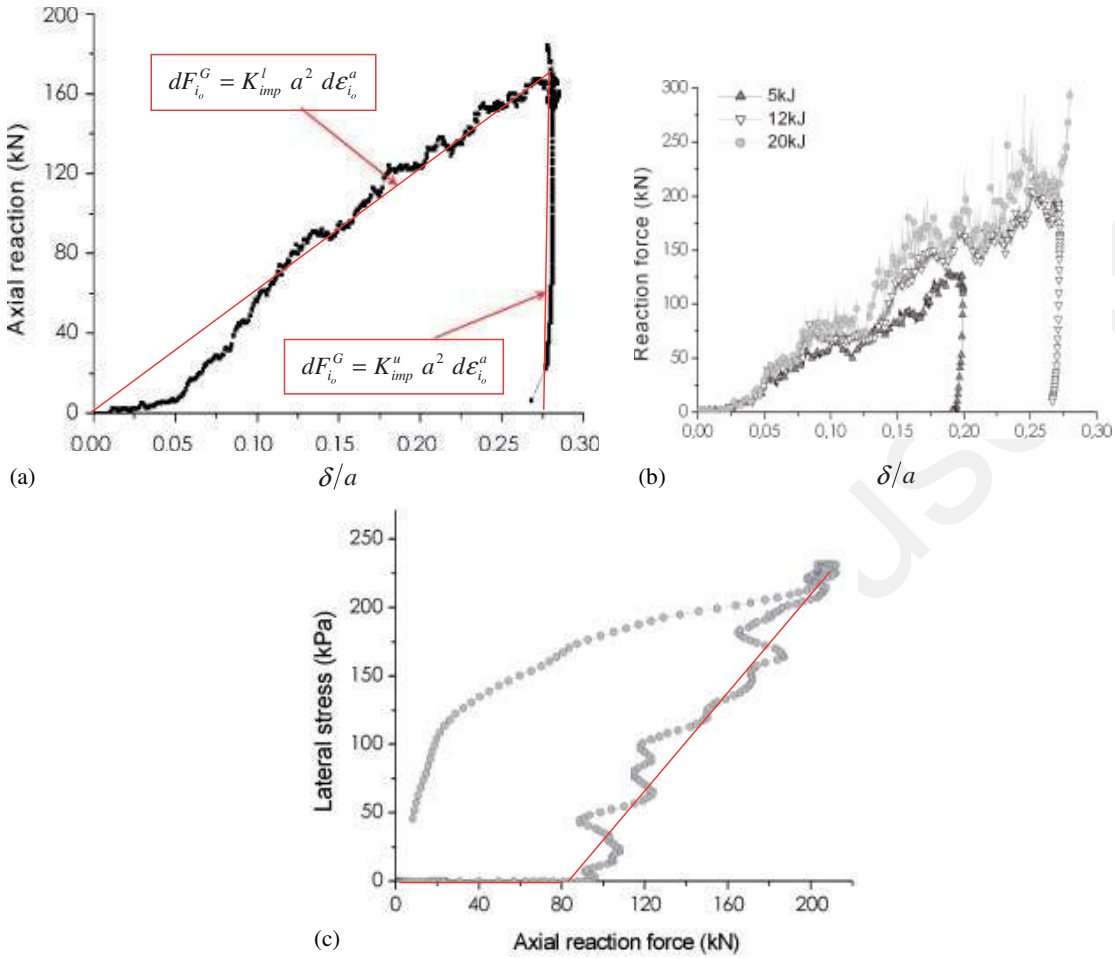

Figure 30. (a) Calibration of a penetration model from the simulation of impacts in confined conditions. Axial reaction force evolution; (b) influence of the boulder's initial kinetic energy on the response of a single cell under impacts in confined conditions; and (c) calibration of a penetration model from the simulation of impacts in confined conditions. Lateral stress evolution.

run by considering three different initial kinetic energy values: 5, 12, and 20 kJ. As seen in Figure 30(b), the boulder's initial kinetic energy is shown to have no significant influence on the evolution of F^G_{i0} in terms of $\varepsilon^{\mathrm{a}}_i$, which authorizes adopting constant values for both the model's parameters $K^{\mathrm{l}}_{\mathrm{imp}}$ and $K^{\mathrm{u}}_{\mathrm{imp}}$. Using Figure 30(a), the calibration of these parameters gives $K^{\mathrm{l}}_{\mathrm{imp}} = 598\,\mathrm{kN/m^2}$ and $K^{\mathrm{u}}_{\mathrm{imp}} = 13\,600\,\mathrm{kN/m^2}$.

Moreover, the evolution of the lateral stress induced by the reaction force onto the four lateral faces (normal to **y** or **z**) of the cell was analysed. As seen in Figure 30(c), this evolution can be described by the following simple bilinear model, where the hysteretic character was omitted:

$$\sigma^l_{i0} = \max\left(0, \eta_{\mathrm{imp}} \frac{F^G_{i0} - \tilde{F}^G_{i0}}{a^2}\right) \tag{32}$$

Table V. Geometric and constitutive parameters used for simulations.

n_x	n_y	n_z	a (mm)	s_x (mm)
8	9	7	500	0
ρ_g (kg/m^3)	Cell porosity (n_c)		μ_c	μ_s
2500	0.40		0.5	0.5

where $\eta_{imp} = 0.47$ and $\tilde{F}_{i_0}^G = 80\,\text{kN}$. These parameters were shown to depend very slightly on the impact velocity for the velocity range considered.

3.3.2. Interaction between soil and lower cells. At the interface between the structure and the soil, the Coulomb friction law is introduced, so that the sliding of the lower cells with respect to the soil can be modelled; this law requires that the friction coefficient μ_s be known. In absence of further experimental investigations, the friction coefficient is chosen equal to 0.5.

3.4. Numerical inspection of the response of a geo-composite cellular structure

3.4.1. Numerical implementation. As the structure is described by a set of nodes, the PFC^{3D} environment can be used again to simulate the response of the structure. A spherical discrete element is affected to each node, and the interacting forces applied to each node, as described in Section 3.2, can be taken into account through specific algorithms developed in FISH programming language [26]. The boulder is described as a single spherical element, and interacting forces develop, as prescribed in Section 3.3, once the boulder penetrates into frontal cells. The resultant of these forces constitutes the reaction force applied by the structure onto the boulder. The displacement of each element can be computed, at each time step of the iterative solving procedure yielding the current position of the boulder, together with the current strained configuration of the structure. It must be noted that in the proposed simulation, the trajectory of the boulder remains parallel to the **x**-direction during the impact.

Subsequently, the different simulations were run by using data reported in Table V. The mass of each cell, affected to the node located at the centre, is given by $m_c = (1 - n_c)\rho_g a^3 = 188\,\text{kg}$, where $n_c = 0.40$ denotes the initial cell porosity.

3.4.2. Influence of the size of the boulder. To investigate the influence of the size of the boulder on the response of the structure, several impact simulations were run with boulders of different diameters (with a same density equal to 2640 kg/m^3), at the same incident kinetic energy equal to 150 kJ. Boulder diameter ranged from 500 mm to 2000 mm. The boulder was initially located at the middle of the front face of the structure: $y_G = n_y a/2$ and $z_G = n_z a/2$. Diameter, mass, and initial velocity of the boulder are reported in Table VI. When the diameter exceeds 500 mm, several cells can be impacted by the boulder.

The response of the structure depends on both the size and the velocity of the boulder (Figure 31). At the beginning of the impact, the boulder penetrates into a single cell whatever its diameter. The impact point is located at the middle of this first impacted cell. As initial velocity decreases when diameter increases, the first peak in the reaction force applied to the boulder also decreases

Table VI. Initial parameters associated with the boulder.

Diameter (mm)	Mass (kg)	Initial velocity (m/s)
500	173	41.67
1000	1382	14.73
1240	2636	10.67
1500	4665	8.02
2000	11 058	5.21

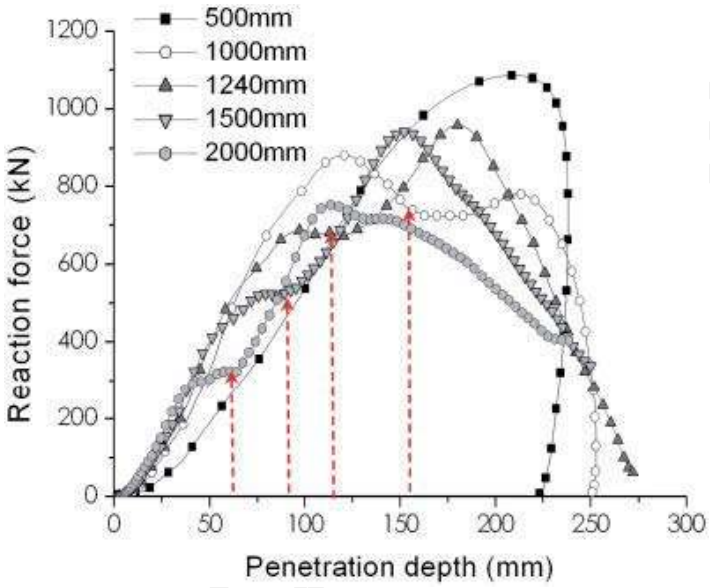

Figure 31. Evolution of the reaction force applied to the boulder in terms of penetration depth. Influence of boulder's diameter. For each boulder diameter considered, the vertical line indicates the occurrence of the impact with type B cells.

when diameter increases. When the penetration depth increases, the boulder is likely to penetrate into other adjoining cells. As seen in Figure 32, this feature depends on the diameter of the boulder. The minimal radii from which a particular type (A, B, C, D, or E) of adjoining cell is impacted are indicated in Figure 32. For a given boulder diameter D_b, the boulder impacts a given type of adjoining cell if the penetration depth exceeds a minimal value given by $p = D_b/2 - \sqrt{(D_b/2)^2 - d_{min}^2}$, where d_{min} denotes the shortest distance between any point of the considered cell and the axis (Gx), G being the centre of the boulder. These minimal values are reported in Table VII for each boulder diameter considered in this section. Thus, for boulder diameters larger than 500 mm, different types of adjoining cells are successively impacted, inducing the step-like evolution of the reaction force applied to the boulder in terms of the penetration depth. In particular, the occurrence of the impact with type B cells can be fairly well detected for the different boulder sizes considered in Figure 31.

Finally, for a given incident kinetic energy, the maximal value of the reaction force applied to the boulder seems not to depend significantly on the size of the boulder. On the contrary, when

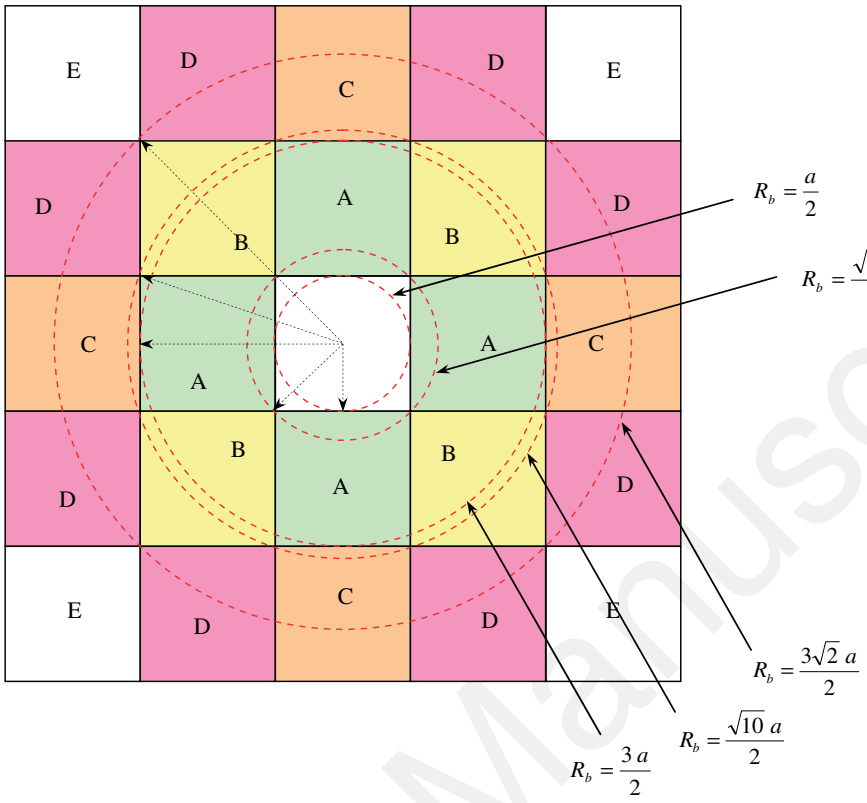

Figure 32. Relation between the boulder radius R_b and the type of adjoining cells impacted.

Table VII. Evolution of the type of cells impacted in terms of the penetration depth p for given boulder diameters D_b.

	Type A	Type B	Type C	Type D	Type E
$D_\mathrm{b} = 500$ mm					
$D_\mathrm{b} = 1000$ mm	$p = 67$ mm	$p = 146$ mm			
$D_\mathrm{b} = 1240$ mm	$p = 53$ mm	$p = 111$ mm			
$D_\mathrm{b} = 1500$ mm	$p = 43$ mm	$p = 89$ mm	$p = 750$ mm		
$D_\mathrm{b} = 2000$ mm	$p = 32$ mm	$p = 65$ mm	$p = 339$ mm	$p = 388$ mm	

the size of the boulder increases, the penetration depth (and thus, the duration of the impact) also increases.

3.4.3. Influence of the boulder's incident kinetic energy. To investigate the influence of the boulder's incident kinetic energy on the response of the structure, several impact simulations were run by considering different initial boulder velocities. Each simulation was carried out with the same boulder, with a diameter of 1 m and a mass of 1382 kg; the boulder is initially located at the middle of the front face of the structure: $y_G = n_y a/2$ and $z_G = n_z a/2$.

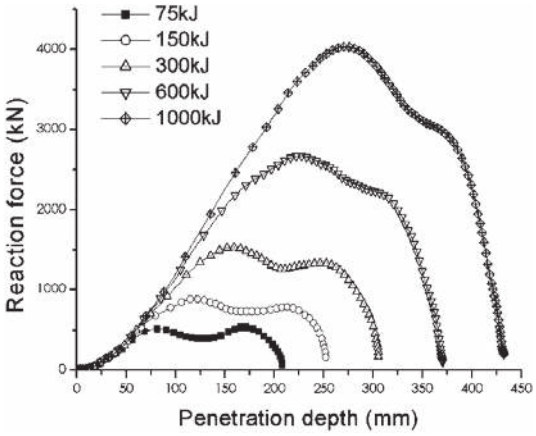

Figure 33. Evolution of the reaction force applied to the boulder in terms of the penetration depth. The second 'bump' occurs for a penetration depth that increases with the boulder's incident kinetic energy.

The incident kinetic energies under consideration ranged from 75 to 1000 kJ. The evolution of the reaction force, for each simulation, is shown in Figure 33. With the investigation presented in Section 3.4.2, it can be conjectured that the second 'bump' observed on the curves in Figure 33 stems from the boulder penetrating a new group of cells. At the beginning of the impact, a single cell is impacted. Depending on the increase in the penetration depth of the boulder, adjoining cells can be penetrated by the boulder. As illustrated in Table VII and Figure 32, the boulder may successively penetrate different adjoining cells, depending on both the boulder diameter and the penetration depth. As shown in Figure 31, the reaction force decreases after the first peak, and then increases once the penetration of adjoining type B cells occurs (the impact with cells type A is difficult to detect). However, the penetration of the boulder within the structure induces relative displacements of the cells in the vicinity of the impact zone. Thus, tangential forces that develop between the first impacted cell and the adjoining cells in contact can be sufficient to move these cells forward, such as type B cells. The penetration of type B cells by the boulder is therefore delayed. This feature is all the more pronounced since the kinetic energy of the boulder is high. As seen in Figure 33, the second 'bump' occurs for penetration depth values that increase with the boulder's incident kinetic energy.

The change in both the maximal reaction force and the maximal penetration depth in terms of the boulder's incident kinetic energy is depicted in Figures 34 and 35. As expected, the maximal reaction force and penetration depth increase with the incident kinetic energy. However, it is worth noting that the curve giving the evolution of the maximal penetration depth is nonlinear. The higher the kinetic energy, the smaller the increase in the maximal penetration depth. This nonlinear feature stems from the inelastic behaviour of the structure. Dissipative mechanisms, related to both the inelastic behaviour of each cell and the sliding phenomenon between adjoining cells, are all increasingly activated as the loading applied by the boulder rises.

3.4.4. Simulation of successive impacts. An important and often debated question on protective structures concerns the residual capacity of such structures after one or more impact events. Indeed, protective structures are meant to last for several decades. They are likely to be subjected to successive rock impacts over their life time, which can reduce their ability to stop future falling

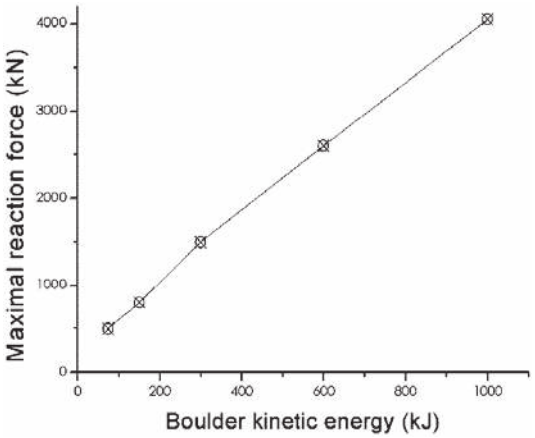

Figure 34. Evolution of the maximal reaction force applied to the boulder in terms of the boulder's incident kinetic energy.

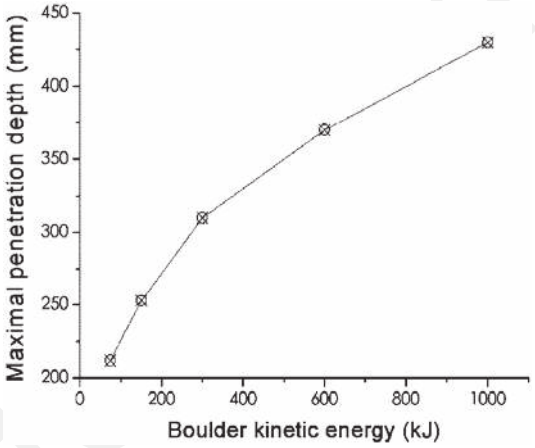

Figure 35. Evolution of the maximal penetration depth in terms of the boulder's incident kinetic energy.

boulders. However, it is always difficult to assess their real residual capacity if one or more impacts have already occurred. This simulation shows the importance of the numerical approach when it comes to providing quantitative information.

To answer this question, the response of a cellular structure subjected to four successive impacts was simulated. Each novel impact is simulated by considering the structure in the residual state obtained at the end of the preceding impact, after removing the boulder.

Each simulation was carried out with a boulder 1 m in diameter and a mass of 1382 kg. The boulder is initially located at the middle of the front face of the structure: $y_G = n_y a/2$ and $z_G = n_z a/2$. The incident kinetic energy was fixed equal to 150 kJ. Complementary data related to the structure are those reported in Table V.

The structure is able to stop the boulder during the three further impacts, but it must be noted that the forces in the structure greatly increase. As shown in Figure 36, the maximal value of the reaction force after a first impact has occurred is significantly higher than that obtained during the

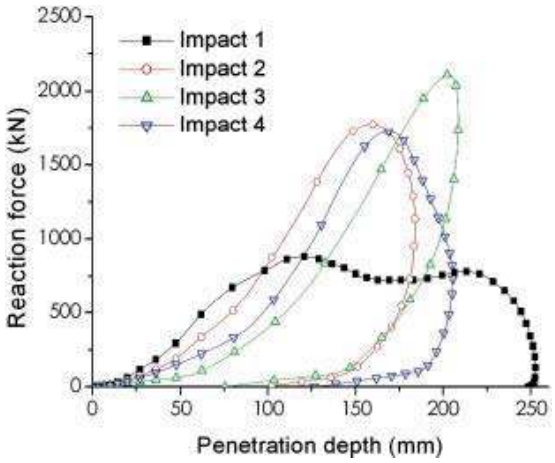

Figure 36. Response of the structure over three successive impacts.

first impact. The peak values and the overall shape of the curves are quite similar for the subsequent impacts. Thus, the first impact, in contrast to the subsequent ones, induces significant changes with respect to the future behaviour of the structure. If further impacts occur corresponding to the same incident kinetic energy, the maximal penetration depth will be shortened and the maximal value of the reaction force will be approximately doubled.

The dissipative capacity of the structure stemming from the relative mobility between adjoining cells is reduced after a first impact has occurred; this increases the stiffness of the entire structure. Therefore, the residual risk related to such a barrier is increased, and the stresses in every part of the structure may be higher. In order to prevent the stresses from dramatically increasing, the dissipative capacity of each single cell should be improved by incorporating specific filling materials. This research is now in progress.

4. CONCLUDING REMARKS

Throughout this paper, a multiscale approach was presented to model the mechanical behaviour of a geo-composite cellular embankment subjected to rockfall impacts. These embankments display a discrete structure on different scales. On the macroscopic scale, these protective structures are composed of an assembly of interacting cells that represent the elementary unit. On the mesoscopic scale, each individual cell can be regarded as a collection of rocky particles in interaction, contained in a metallic netting box. This striking feature justifies that a discrete description of the bodies be adopted on the different relevant scales of the problem at hand.

In the context of a multiscale approach, the constitutive behaviour of each cell was first analysed separately, and constitutive relations were developed to describe the behaviour of a given cell under confined compressive loading paths. Both the rocky filling material and the containing netting box, in close interaction, were described by using a discrete element method in the PFC^{3D} environment. Realistic shapes of rocky particles were taken into account by creating unbreakable agglomerates of spherical elements (clumps). As a first approximation, the local damage that is likely to occur in the neighbourhood of contact areas between adjoining particles was modelled through an elastic–perfectly plastic contact law in the normal direction of contacts.

Parameters introduced in the simulation of both the wire netting box and the filling material were calibrated along specific loading paths in quasi-static conditions (tensile tests on plane wire net sheets and confined compressive tests on gabion cells) from the comparison between both experimental and numerical results. Further simulations under different loading conditions (see also [31]) have provided encouraging elements of validation, confirming the robustness and the relevance of the approach proposed. In particular, the model was shown to be able to reproduce the response of a cell subjected to dynamical impacts under confined and unconfined conditions fairly well.

Then a computational tool for simulating the response of a geo-composite cellular structure during boulder impacts was developed in the PFC^{3D} environment. The structure was described by a set of nodes associated with each cell. Interacting forces that exist between adjoining cells were accounted for by implementing the constitutive relations identified on the individual cell scale. As a first assumption, the analysis was restricted to the case of boulders' incident trajectories perpendicular to the front face of upstream cells. Further research is now in progress to extend the simulation to any type of incident trajectory.

As a first illustration of the capability of such multiscale approaches, successive impacts were simulated. The first impact was shown to be the most prejudicial one in the sense that it induces both rheological and geometrical changes within the structure that significantly modify its future behaviour under impacts. Finally, this engineering tool should contribute to a more optimized design and a better conception of this type of protective structure, and thereby to better management of the risk involved.

APPENDIX A

Let two clumps in contact be considered at a given stage of the loading. As the contact occurs between two constitutive spherical particles, the analysis can be restricted by considering two contacting spheres. The current radii of the two spheres are denoted R_1 and R_2. As suggested in Section 2.2.2, superficial damage may develop within the superficial crown of the particles. This phenomenon can be accompanied by removal of matter (attrition mechanism), leading to a decrease in the particle radii. This reduction can be modelled from the volume overlapped by the two spheres. The overlapping volume is the sum of two volumes, v_{ABI} and v_{ABJ}, which are a function of δ_1 and δ_2, respectively (Figure A1):

$$v_{ABJ}(\delta_1) = \frac{\pi}{3}(3R_1 - \delta_1)\delta_1^2 \tag{A1}$$

$$v_{ABI}(\delta_2) = \frac{\pi}{3}(3R_2 - \delta_2)\delta_2^2 \tag{A2}$$

where

$$\delta_1 = \frac{(2R_2 - \delta)\delta}{2(R_1 + R_2 - \delta)} \quad \text{and} \quad \delta_2 = \frac{(2R_1 - \delta)\delta}{2(R_1 + R_2 - \delta)}$$

The overlapping distance $\lambda = u^{\mathrm{n}}$ between the two spheres can be resolved into an elastic part $\lambda_{\mathrm{e}} = u_{\mathrm{e}}^{\mathrm{n}}$ and a plastic counterpart $\lambda_{\mathrm{p}} = u_{\mathrm{p}}^{\mathrm{n}}$, as described by Equations (16)–(17). Thus, the volume of removed matter, for each particle, is assessed from the plastic components $\delta_{1,\mathrm{p}}$ and $\delta_{2,\mathrm{p}}$

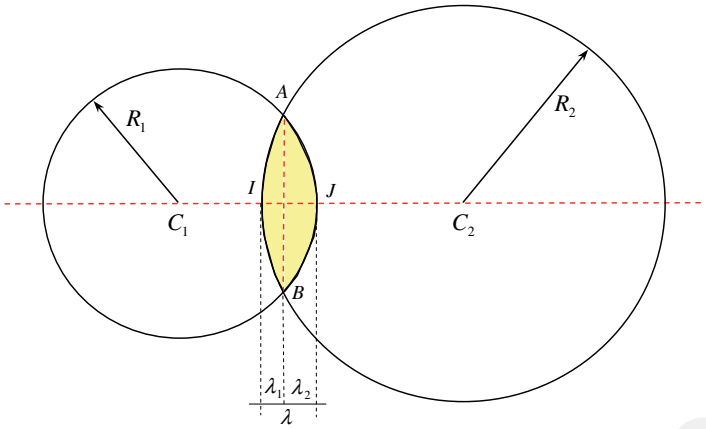

Figure A1. Overlapping between two contacting spheres.

as follows:

$$v_{ABJ}(\delta_{1,\mathrm{p}}) = \frac{\pi}{3}(3R_1 - \delta_{1,\mathrm{p}})\delta_{1,\mathrm{p}}^2 \tag{A3}$$

$$v_{ABI}(\delta_{2,\mathrm{p}}) = \frac{\pi}{3}(3R_1 - \delta_{2,\mathrm{p}})\delta_{2,\mathrm{p}}^2 \tag{A4}$$

Then the thicknesses ΔR_1 and ΔR_2 of the removed crowns are determined as follows:

$$\tfrac{4}{3}\pi R_1^3 - \tfrac{4}{3}\pi(R_1 - \Delta R_1)^3 = v_{ABJ}(\delta_{1,\mathrm{p}}) \tag{A5}$$

$$\tfrac{4}{3}\pi R_2^3 - \tfrac{4}{3}\pi(R_2 - \Delta R_2)^3 = v_{ABI}(\delta_{2,\mathrm{p}}) \tag{A6}$$

Moreover, by noting that $\frac{4}{3}\pi R_i^3 - \frac{4}{3}\pi(R_i - \Delta R_i)^3 \approx 4\pi R_i^2 \Delta R_i$ $(i = 1, 2)$, ΔR_1 and ΔR_2 are expressed as

$$\Delta R_1 = \frac{v_{ABJ}(\delta_{1,\mathrm{p}})}{4\pi R_1^2} \tag{A7}$$

$$\Delta R_2 = \frac{v_{ABI}(\delta_{2,\mathrm{p}})}{4\pi R_2^2} \tag{A8}$$

The procedure is applied at each step of the loading, updating the radii of the constitutive spheres of the particles. Thus, progressive erosion can be modelled. To prevent any numerical instability, a constitutive sphere is definitively suppressed if its current radius is equal to 10% of the initial value before reduction.

ACKNOWLEDGEMENTS

This research has been partially supported by the private partner France-Macaferri (F. Derache, F. Ferraiolo). The support of both the research consortium RNVO and the PGRN (Natural Hazard Pole of Grenoble), as well as the technical assistance supplied by the Technological University Institute of Grenoble (M. A. Petrone) are gratefully acknowledged by the authors.

REFERENCES

1. Descoeudres F. Aspects géomécaniques des instabilités de falaises rocheuses et des chutes de blocs. *PUBLICATIONS de la société suisse de Mécanique des Sols et des Roches*, Montreux (Suisse), 1997; 3–11.
2. Gotteland P, Lambert S, Balachowski L. Strength characteristics of tire chips sand mixtures. *Studia Geotechnica et Mechanica* 2005; **27**(1–2):55–66.
3. Hearn G *et al.* Testing and modelling of two rockfall barriers. *Transportation Research Record* 1995; **1504**:1–11.
4. Peila D, Castiglia C, Oggeri C, Guasti G, Recalcati P, Sassudelli F. Full scale tests on geogrid reinforced embankments for rockfall protection. *2nd European Geosynthetics Conference*, Eurogeo II, 2000; 317–322.
5. Peila D, Oggeri C, Castiglia C, Recalcati P, Rimoldi P. Testing and modelling geogrid reinforced soil embankments subject to high energy rock impact. *7th International Conference on Geosynthetics*, Nice. Balkema: Rotterdam, 2002; 133–136.
6. Pichler B, Hellmich Ch, Mang HA. Impact of rocks onto gravel, design and evaluation of experiments. *International Journal of Impact Engineering* 2005; **31**(5):559–578.
7. Nicot F. From constitutive modelling of a snowcover to the design of flexible structures. Part I, Mechanical modelling. *International Journal of Solids and Structures* 2004; **41**:3317–3337.
8. Nicot F. From constitutive modelling of a snowcover to the design of flexible structures. Part II, Some numerical aspects. *International Journal of Solids and Structures* 2004; **41**:3339–3352.
9. Tran TH, Dedecker F, Cambou B. Discrete creep model for long-term behavior of rock-fill dams. In *Powders and Grains 2005*, Herrman R-G, McNamara S (eds). Balkema: Rotterdam, 2005; 681–685.
10. Oda M. The mechanism of fabric changes during compressional deformation of sand. *Soils and Foundations* 1972; **12**:1–23.
11. Oda M, Konishi J. Microscopic deformation mechanism of granular material in simple shear. *Soils and Foundations* 1974; **14**(4):15–32.
12. Mehrabadi MM, Cowin SC. Initial planar deformation of dilatant granular materials. *Journal of the Mechanics and Physics of Solids* 1978; **26**:269–284.
13. Mehrabadi MM, Oda M, Nemat-Nasser S. On statistical description of stress and fabric in granular materials. *International Journal for Numerical and Analytical Methods in Geomechanics* 1982; **6**:95–108.
14. Satake M. Constitution of mechanics of granular materials through graph representation. *Theoretical And Applied Mechanics*, vol. 26. University of Tokyo Press: Tokyo, 1978; 257–266.
15. Satake M. Fabric tensor in granular materials. *IUTAM Conference on Deformation and Failure of Granular Materials*, Delft, 1982; 63–68.
16. Nemat-Nasser S, Mehrabadi MM, Iwakuma T. On certain macroscopic and microscopic aspects of plastic flow of ductile materials. In *Three-dimensional Constitutive Relations and Ductile Fracture*, Nemat-Nasser S (ed.). North Holland: Amsterdam, 1981; 157–172.
17. Nemat-Nasser S, Mehrabadi MM. Stress and fabric in granular masses. In *Mechanics of Granular Materials. New Models and Constitutive Relations*, Jenkins JT, Satake M (eds). Elsevier: Amsterdam, 1983; 1–8.
18. Chang CS. Micromechanical modelling of deformation and failure for granulates with frictional contacts. *Mechanics of Materials* 1992; **16**:13–24.
19. Chang CS, Liao CL. Estimates of elastic modulus for media of randomly packed granulates. *Applied Mechanics Review* 1994; **47**:197–206.
20. Cambou B, Dubujet P, Emeriault F, Sidoroff F. Homogenization for granular materials. *European Journal of Mechanics, A/Solids* 1995; **14**(2):255–276.
21. Cambou B, Chaze M, Dedecker F. Change of scale in granular materials. *European Journal of Mechanics, A/Solids* 2000; **19**:999–1014.
22. Nicot F, Darve F. A multiscale approach to granular materials. *Mechanics of Materials* 2005; **37**(9):980–1006.
23. Darve F, Nicot F. On incremental non linearity in granular media: phenomenological and multi-scale views (Part I). *International Journal for Numerical and Analytical Methods in Geomechanics* 2005; **29**:1387–1409.
24. Darve F, Nicot F. On flow rule in granular media: phenomenological and multi-scale views (Part II). *International Journal for Numerical and Analytical Methods in Geomechanics* 2005; **29**:1411–1432.
25. Cundall PA, Roger DH. Numerical modelling of discontinua. *Engineering computations* 1992; **9**:101–113.
26. ITASCA Consulting Group. Particle Flow Code in three dimensions (2003), theory and background, FISH in PFC. *User's Guide*. ITASCA Consulting Group: Mineapolis, U.S.A., 2003.
27. Cundall PA, Strack ODL. A discrete numerical model for granular assemblies. *Géotechnique* 1979; **29**:47–65.

28. Nicot F, Cambou B, Mazzoleni G. From a constitutive modelling of metallic rings to the design of rockfall restraining nets. *International Journal for Numerical and Analytical Methods in Geomechanics* 2001; **25**(25):49–70.
29. Nicot F, Boutillier M, Gagliardini O. Modelling of a snowpack in interaction with a flexible structure using a coupled Lagrangian-Discrete approach. *International Journal for Numerical and Analytical Methods in Geomechanics* 2003; **27**:259–274.
30. Taylor GI. The mechanism of plastic deformation of crystals—I, Theoretical. *Proceedings of the Royal Society of London*, *Series A* 1934; **145**:362–387.
31. Bertrand D, Nicot F, Gotteland P, Lambert S. Modelling a geo-composite cell using discrete analysis. *Computers and Geotechnics* 2005; **32**:564–577.
32. Velinsky SA. General nonlinear theory for complex wire rope. *International Journal of Mechanical Science* 1985; **27**:497–505.
33. AFNOR. *NF P 94-325-1:Exécution des travaux géotechniques spéciaux, ouvrages en gabions, ouvrages hors site aquatique*. AFNOR: Paris, 2004; 24.
34. Bertrand D, Gotteland P, Nicot F. DEM modelling of natural stones assembly confined in wire mesh. In *Powders and Grains 2005*, Herrman R-G, McNamara S (eds). Balkema: Rotterdam, 2005; 681–685.
35. Thornton C, Yin KK. Impact of elastic spheres with and without adhesion. *Powder Technology* 1991; **65**:153–166.
36. Bardet JP. Introduction to computational granular mechanics. In *Behaviour of Granular Materials*, Cambou B (ed.). Springer: Wien, New York, 1998; 99–169.
37. Briggs C, Evertsson C. Shape potential of rock. *Minerals Engineering* 1998; **11**(2):125–132.
38. Liu HY, Kou SQ, Lindqvist P-A. Numerical studies on the inter-particle breakage of a confined particle assembly in rock crushing. *Mechanics of Materials* 2005; **37**(9):935–954.
39. Nemat-Nasser S, Horii H. Compression-induced non-planar crack extension with application to splitting, exfoliation and rock burst. *Journal of Geophysical Research* 1982; **87**:6805–6821.
40. Horne MR. The behaviour of an assembly of rotund, rigid cohesionless particles—I, II. *Proceedings of the Royal Society of London*, vol. 286. 1965; 62–97.
41. Radjai F, Wolf D, Jean M, Moreau JJ. Bimodal character of stress transmission in granular packing. *Physical Review Letters* 1998; **80**(1):61–64.
42. Dantu P. Contribution àl'étude mécanique et géométrique des milieux pulvérulents. *Proceedings of the 4th International Conference on Soil Mechanics Foundation and Engineering*, London, vol. 1, 1957; 144.
43. Drescher A. An experimental investigation of flow rules for granular materials using optically sensitive glass particles. *Géotechnique* 1976; **26**:591–601.
44. Oda M, Konishi J, Nemat-Nasser S. Experimental evaluation of strength of granular materials, effects of particle rolling. *Mechanics of Materials* 1982; **1**:269–283.
45. Lambert S, Gotteland P, Ple O, Bertrand D, Nicot F. Modélisation du comportement mécanique des cellules de matériaux confines. *Journée Nationale de Géotechnique et de Géologie* 2004; 219–226.
46. Arthur JRF, Manzies BK. Inherent anisotropy in a sand. *Géotechnique* 1972; **22**(1):115–128.
47. Arthur JRF, Phillips AB. Homogeneous and layered sand in triaxial compression. *Géotechnique* 1975; **25**(4):799–815.
48. Lambert S, Gotteland P, Bertrand D, Nicot F. Comportement mécanique de géo-cellules impactées, applications aux ouvrages pare-blocs. *27ème Journées Nationales de Géotechnique et de Géologie* 2006; 121–128.
49. Smith DD, Duffy JD. Field tests and evaluation of rockfall restraining nets. *Final Report*, California Department of Transportation, 1990.